UCLouvain

École polytechnique de Louvain

Estimating storm surge and coastal inundation induced by tropical cyclones in the Great Barrier Reef

Author: **Max WIBERG**
Supervisors: **Emmanuel HANERT, Jonathan LAMBRECHTS**
Readers: **Vincent LEGAT, Christopher THOMAS**
Academic year 2024–2025
Master [120] in Mechanical Engineering

Abstract

As the severity of tropical cyclones (TCs) is likely to increase and the sea level rises due to climate change, destructive storm surges are expected to be more frequent. It becomes increasingly important to be able to forecast their impact. The use of reliable storm surge models will be a valuable resource in the effort to predict the consequences of a cyclone making landfall. Northern Australia, situated near the southern tropical line, is subject to numerous TCs, formed in warm waters. In this study we focus on the coastal area around the Great Barrier Reef in northern Australia, which is also of special interest due to its bathymetry and the seabed rugosity. We analyze through a set of simulations the case of cyclone Yasi, a category 5 TC which hit this area in 2011. We use the 2D SLIM (Second-generation Louvain-la-Neuve Ice-ocean Model) hydrodynamic model with a wetting and drying setup to estimate the storm surge and coastal inundation induced by cyclone Yasi. The results obtained show that SLIM performs well under certain circumstances: the wind speed and atmospheric pressure profiles must be constructed with a cyclone model such as Holland's and the simulation mesh needs to be sufficiently refined near the coast and along the cyclone track. As SLIM might be used for large-scale modeling of storm surges, we highlight the interaction between tide and storm surge. The model presents a few limitations but overall it shows potential for future applications in storm surge modeling.

Acknowledgements

I would like to thank everyone who contributed to the completion of this thesis.

First, I thank my supervisor, Emmanuel Hanert for his patience, his availability and his guidance throughout the year. I also thank my co-supervisor, Jonathan Lambrechts, and his team for their support and quick responses to issues with SLIM.

Thanks to Vincent Legat for agreeing to read this work and to Christopher Thomas for his valuable feedback and guidance.

I thank the entire SLIM team – Thomas, Colin, Lauranne, Riana, Amaury, Douchan, Alexis and Mattias - for their general support and feedback during this project. A special thanks to Thomas for his reactivity and helping me solve many bugs.

I am immensely grateful to my parents for their love and encouragement, and to my friends Robin, Philip, Geoffrey and Walter for their constant support. Finally, a heartfelt thanks to Romane for reassuring and motivating me during tough times.

Contents

Chapter 1

Introduction

Extreme storms such as tropical cyclones, bring huge devastation in their aftermath. The high wind speed, the heavy rains and the large storm surge provoke great damage to infrastructure and lead to human losses. With global warming likely to increase the proportion of severe cyclones (IPCC, 2021), it becomes increasingly important to be able to forecast their impact.

1.1 Tropical cyclones

Tropical cyclones (TCs), also known as typhoons or hurricanes depending on the region, cause widespread destruction particularly in coastal and low-lying areas. A storm surge can inundate vast areas, leading to catastrophic flooding. Combined with winds exceeding 150 km/h and rainfall that can reach over 200 mm in a single day, these factors make TCs some of the most devastating natural disasters.

TCs form under specific meteorological conditions. These are, in a simplified explanation, the presence of large amounts of water (ocean) and this water being warm enough, the breaking point is usually considered to be around +27°C (Gray, 1998). Regions near the tropical lines, are regions that receive much heat from the sun. Because of the spherical shape of the Earth and the incline of its rotation axis, the angle of the incident radiation from the sun allows a greater heat accumulation in these regions. Therefore the tropical regions are favorable for the genesis of a cyclone (hence the name tropical cyclone). These cyclones have varying intensity, and are often classified into 5 categories using the Saffir-Simpson scale, ranging from 1 for the weakest TCs with wind speed between 119 km/h and 153 km/h, to 5 for which the wind speed is over 252 km/h (National Hurricane Center, NHC).

Figure 1.1: Flooding cause by storm surge of Hurricane Katrina in New Orleans, Louisiana. (Source: NOAA)

With the climate changing due to anthropogenic activities, the oceans are warming. A higher sea surface temperature provides more energy for the storm to gain strength. Cyclones forming over very warm waters (30°C or higher) are more likely to intensify into categories 3 to 5 (IPCC, 2021).

The wind from a cyclone is devastating, but for some cyclones, the biggest threat is the water pushed by the wind as storm surge and the flooding caused by rains. A storm surge is a response by the ocean to the meteorological conditions and the bathymetry. The atmospheric pressure drop of the cyclone (in its eye) applies an upward force on the water surface, while the winds pushes the water inland. These two components, induce a large wave called storm surge. This wave provokes inundations in the coastal areas. In Figure 1.1 we can see the large flooding caused by Cyclone Katrina, one of the most destructive in the United States, killing nearly 1400 people, in Louisiana, most of the deaths were due to the large storm surge that reached a height of about 8 m in some locations (Knabb et al., 2023). A schematic of the storm surge phenomenon is given in Figure 1.2. In addition, rising sea levels caused by melting ice caps amplify the threat posed by cyclones. Higher sea levels lead to more devastating storm surges and coastal inundation, increasing the vulnerability of low-lying regions to extreme flooding events (IPCC, 2021).

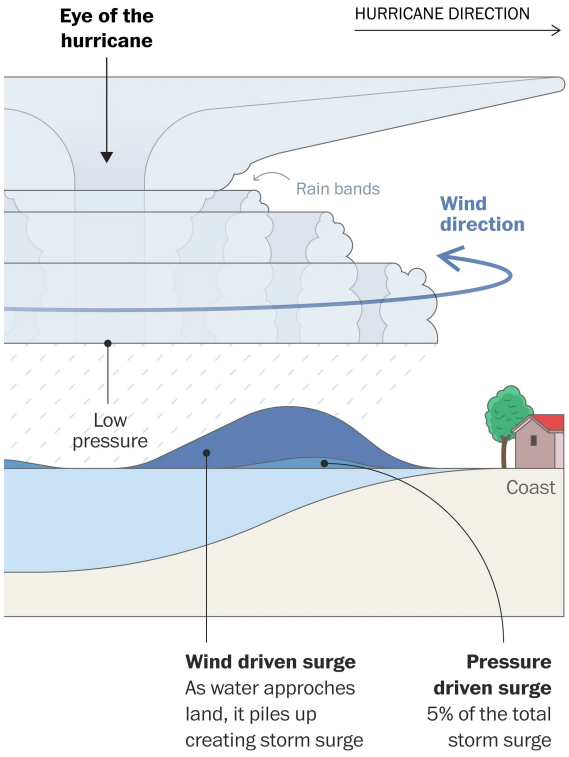

Figure 1.2: Schematic explanation of how a storm surge works. From the National Oceanic and Atmospheric Administration (NOAA).

1.2 Australia and the Great Barrier Reef

Due to its location, near the southern tropic line, northern Australia is strongly subject to cyclones. Historical records show numerous occurrences of TCs in the north of Australia, as illustrated in Figure 1.3. When looking at the population density in Australia, shown in Figure 1.4, we observe that the east coast is the most populated region. Thus, combining the fact that the TCs occur on the northern side of Australia with the high population density on the east coast, we find it natural to make this our study area. We focus on the area of the Great Barrier Reef (GBR) situated in northeastern Australia (although less populated than the southeast area).

The Great Barrier Reef (GBR) is known for its remarkable variety of species, and is a unique ecosystem. However, in the case of storm surge modeling the interesting specific features of the GBR are its bathymetry (Figure 1.5) and the seabed rugosity (Delandmeter et al., 2017; Lambrechts et al., 2008).

Queensland, the region on the coast next to the GBR, has been struck by

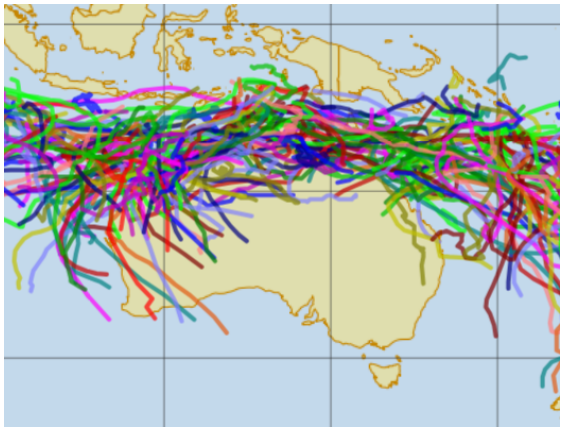

Figure 1.3: Map of past tropical cyclones tracks from The Australian Bureau of Meteorology from 1999 to 2023 Australian Bureau of Meteorology (BoM), 2023.

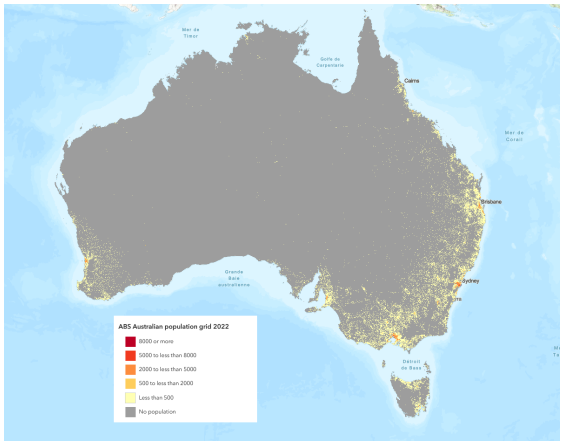

Figure 1.4: Density of the population in Australia in 2022 (Commonwealth of Australia (Geoscience Australia), 2021).

several devastating cyclones in the past years. In February 2015, the severe cyclone Marcia wreaked destruction over Queensland. Several population centers of the region, including Rockhampton and Yeppoon, were flooded. Figure 1.6 gives a more detailed route for the cyclone. Nearly 2000 properties were damaged. According to the Australian Institute for Disaster Resilience (AIDR), the Insurance Council of Australia estimated insured damage to the figure of 403.6 million AUD, about 265 million USD (Australian Institute for Disaster Resilience, 2015). A few years earlier, cyclone Yasi made landfall on the city of Cardwell, the track of the cyclone is represented in Figure 1.7. In Cardwell a storm surge of 5 m was measured. Figure 1.8 shows a local example of the damage such a surge can make. Yasi caused the death of one person. Overall it generated approximately 3.6 billion USD worth of damage, with the AIDR estimating insurance costs up to 1.41 billion

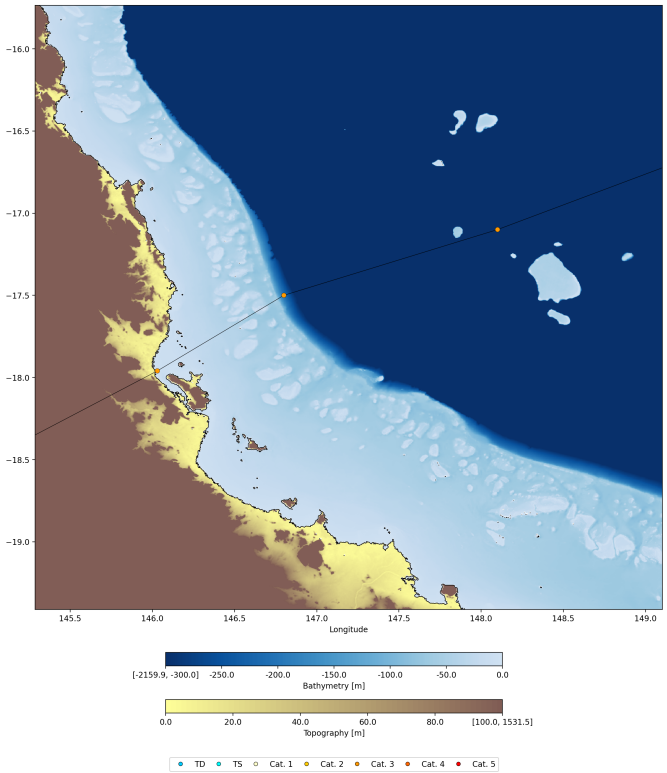

Figure 1.5: Deepreef bathymetry (blue) and topography (brown to yellow) in the GBR, close-up on the region around which Yasi made landfall, track of Yasi in Saffir-Simpson scale (Beaman, 2010; Taylor et al., 2010).

USD (Australian Institute for Disaster Resilience, 2011; Government, 2012). This highlights again the importance of modeling storm surges and impacts of cyclones, for authorities, risk managers, insurers and scientists with in interest in coastal regions.

1.3 Storm surge modeling

Storm surge modeling is an efficient and necessary tool to study and forecast the behavior of coastal flooding caused by tropical cyclones. Storm surge models simulate the ocean's response to a storm. They provide information on predicted water levels with the aim to locate possible inundated areas.

The results from such models can be used in three ways. First for a deterministic approach, where a single cyclone is modeled and the simulated storm surge for that cyclone is obtained. Then for a probabilistic approach, we run

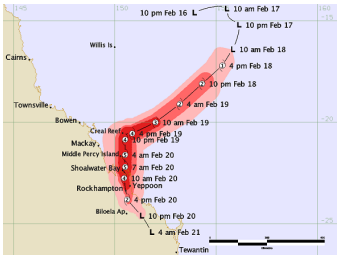

Figure 1.6: Track of the Tropical Cyclone Marcia (2015) from the Bureau of Meteorology (BOM).

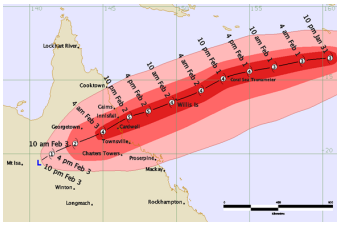

Figure 1.7: Track of the Tropical Cyclone Yasi (2011) from the Bureau of Meteorology (BOM).

Figure 1.8: Jetty broken in Cardwell (Source: DSITIA).

simulations for a large set of cyclones, and statistically analyze the results of the simulations, to find the probability of surge height at different locations. Then for more advanced results the model can be used to form an ensemble prediction, by running 100 to 1000 simulations with different (existing and simulated) cyclones, using a cyclone genesis prediction as in Arthur, 2021). These simulations allow for finding the maximal water height possible at each location, thus being very useful for risk managers (National Oceanic and Atmospheric Administration, (NOAA)).

Several different storm surge models exist. From these we can cite SLOSH (the Sea, Lake, and Overland Surges from Hurricanes) using a finite difference method, and the ADCIRC model (ADvanced CIRCulation) that is more sophisticated as it uses an unstructured grid (CIRCulation, (ADCIRC); Jelesnianski et al., 1992). The SLOSH model is used by the NOAA for their forecasting (National Oceanic and Atmospheric Administration, (NOAA)).

In this research we are going to use SLIM (Second-generation Louvain-la-Neuve Ice-ocean Model - https://www.slim-ocean.be/). SLIM uses the Discontinuous Galerkin finite element method, providing it a high precision. This model was validated for several uses, including larvae dispersal, coral connectivity analysis, tracing pollutants and sediments (Faryuni et al., 2024; Figueiredo et al., 2022; Sterckx et al., 2023; Wolanski et al., 2021). It has however not been validated for storm surge modeling.

1.4 Objectives

The main goal of this project is to **analyze if SLIM performs well as a storm surge model**, as it has not been validated for such use. To do this, we use a deterministic approach to analyze the case of cyclone Yasi through a set of simulations, searching for the best wind profile option and we will also **test the model for different mesh resolutions** to investigate how the coarsening of the mesh impacts the model's results in terms of storm surge and size of inundated areas.

As in the future we might explore the use of SLIM for a probabilistic approach or an ensemble approach, with the aim to build risk maps of the GBR area, we also **investigate the interaction between the tidal cycle and the storm surge**.

In our model we will use SLIM with a wetting and drying method, to model the hydrodynamics of the ocean. For the cyclone dynamics we are going to test our model with the Holland's (Holland, 1980) model for tropical cyclones. Our model will cover an area centered around the track of cyclone Yasi and will cover both land and ocean. All of these steps and methods will be covered thoroughly. After the presentation of the simulations results, we will discuss their implications in relation to the objectives mentioned above.

Chapter 2

Materials and methods

The main objective of the project is, as mentioned before, to find out how our model simulates flooding due to storm surge. In this chapter, we will explore the methods used to achieve these results and the different tools that we are going to use.

All simulations will be made using SLIM, a multiscale model of the land-sea continuum. SLIM is composed of many branches, such as SLIM1D, used to compute flows in rivers, SLIM2D, used in studies of shallow barotropic flows (flows that have parallel pressure and density gradients) and SLIM3D, which is computationally more expensive and may be used for more complex situations where the vertical aspects of the flow cannot be neglected. SLIM also offers a variety of features, such as a Langragian particle tracker (for larvae or debris tracking) and an Eulerian transport model (for tracers dynamics such as pollutants and sediments). In this case, we are going to use SLIM2D, with a wetting and drying setup, which allows us to simulate the flows over areas where there is no water initially. This is of course mandatory in our case since we study inundation.

2.1 SLIM2D

SLIM2D is sufficient due to the limited depth of the area between the Queensland coastline and the Great Barrier Reef, which is why we will not use SLIM3D. We briefly cover the hydrodynamic equations that will be the main point of the calculations, present a special functioning mode of the model relevant to our case, and then cover the numerical aspects of the resolution and the forcing data that we insert into the model.

2.1.1 Hydrodynamic model equations

The governing equations of the flow in this case are the shallow water equations. They are derived by depth-averaging the Navier-Stokes equations using the following steps and assumptions (Lambrechts et al., 2008, Gourgue et al., 2013):

- Incompressibility of the flow,
- Hydrostatic balance of the pressure,
- Vertical homogeneity.

The resulting 2D equations read:

$$\frac{\partial \eta}{\partial t} + \nabla \cdot (H\mathbf{u}) = 0 \tag{2.1}$$

$$\frac{\partial \mathbf{u}}{\partial t} + \mathbf{u} \cdot (\nabla \mathbf{u}) + f\boldsymbol{k} \times \mathbf{u} = -g\nabla\eta - \frac{1}{\rho}\nabla p_{atm} + \frac{1}{H}\nabla \cdot (H\nu(\nabla \mathbf{u})) + \frac{\boldsymbol{\tau^s} - \boldsymbol{\tau^b}}{\rho H} \tag{2.2}$$

In the shallow water equations, we define the following variables and parameters. The time is denoted by t $[s]$. The reference height of the water column, also referred to as the bathymetry, is h $[m]$. Above this reference height, the water surface elevation is represented by η $[m]$. The actual water depth H $[m]$ is given by $H = \eta + h$. The horizontal velocity vector $\mathbf{u} = (u, v)$ $[m\,s^{-1}]$ provides the eastward (u) and northward (v) components. The Coriolis parameter f $[s^{-1}]$ is expressed as $f = 2\,\omega \sin(\phi)$, with ω $[rad\,s^{-1}]$ denoting the Earth's angular velocity and ϕ the latitude $[rad]$. We let $\mathbf{k}$ be the upward unit vector, while g $[m\,s^{-2}]$ represents the gravitational acceleration. The parameter ν $[m^2\,s^{-1}]$ is the horizontal eddy viscosity computed with the Smagorinsky parametrization (Smagorinsky, 1963). ρ $[kg\,m^{-3}]$ denotes the density of water. p_{atm} $[Pa]$ is the atmospheric pressure at the water surface. The surface stress vector $\boldsymbol{\tau^s}$ $[N\,m^{-2}]$ will be explained in detail later in this chapter. The bottom stress vector $\boldsymbol{\tau^b}$ $[N\,m^{-2}]$ is computed with the Chézy-Manning-Strickler formula which reads:

$$\boldsymbol{\tau^b} = \rho g n^2 \frac{\mathbf{u}|\mathbf{u}|}{H^{1/3}} \tag{2.3}$$

Where n is the Manning coefficient, We have three different values for this coefficient, we use 0.025 in the sea considering a sandy seabed, we multiply this by 3.16 over reefs (Delandmeter et al., 2017), and on land we consider short grass which has an estimated Manning coefficient of 0.022 (Arcement and Schneider, 1990).

The model equations are solved numerically, therefore the variables needs to be discretized. On the one hand, we have a temporal discretization with an explicit

numerical integration scheme. On the other hand we have a spatial discretization, the domain is spatially divided in small triangles, and together they form a mesh. The mesh has an important role in the precision of the results. If it is too coarse, the computation will be fast but the result may lose some precision, on the other hand if it is too fine, it may lead to unnecessary long computation times (Saint-Amand et al., 2023).

2.1.2 Wetting and drying

These equations work fine for most cases but they have a liability in the regions where the water depth H is 0 or almost 0. This induces a division by 0 in the right term of equation 2.2. This is crucial for our application since we want to compute the arrival of the flow on the land, i.e. from a region with positive topography without water to a region that is submerged by the water. To solve this problem, SLIM2D can be used with a wetting and drying method. There are a few different types of methods that can be used to deal with this issue Gourgue et al., 2009; Ortleb et al., 2022. In this case, the method allows us to use the same conditions as if we were using the regular hydrodynamic equations and this without causing stability perturbations, by always maintaining a minimal water level H_{lim} we impose on each element.

In this case the temporal scheme obey the following equation:

$$U^{n+1} = U^n + \Delta t M^{-1} F(U^n) \tag{2.4}$$

with M the mass matrix and F is the flux. Equation 2.1 is:

$$\eta^{n+1} = \eta^n + \Delta t M^{-1} F(\eta^*, \bar{\mathbf{u}}^*) \tag{2.5}$$

The wetting and drying method used for this project undergoes four steps (Randresihaja et al., 2025). First it computes the flux leaving the element F^{ext}. Then if an excessive amount of water leaves the triangle, a limiting coefficient is computed to reduce the flux, this coefficient is parametrized so that $H > H_{lim}$ on average on the triangle. Then it computes all the fluxes with that limiting coefficient, and finally it verifies that $H > H_{lim}$ on each vertex of the element. If a vertex doesn't fulfill that condition, another limiter is applied to redistribute the mass within the element.

2.1.3 Domain and meshing

The geographical domain defined for the simulations in this project is presented in Figure 2.1. The region is centered around the track of TC Yasi given by the Joint

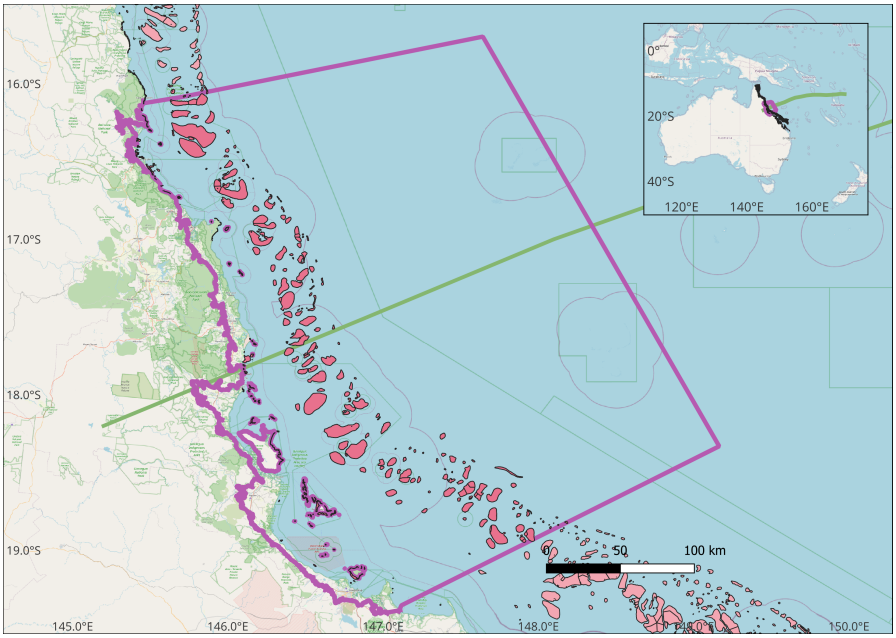

Figure 2.1: Simulation domain boundaries (purple) with Yasi track (green) and reefs inside (pink) and reefs outside of the domain (lighter pink) (OpenStreetMap Contributors, 2024).

Typhoon Warning Center (JTWC), 2023, in green, and delimited by the purple line, the boundary of the domain. We have what we consider open boundaries that are allowed to receive forcings such as currents. These are the boundaries in the ocean (straight lines in the figure). We also have the closed boundary that is on land and therefore isn't allowed to give or receive any forcing. The closed boundary is chosen by taking the SRTM30 (Shuttle Radar Topography Mission from NASA) Digital Elevation Model (DEM) with the Opentopography API, (NASA, 2000; OpenTopography, 2024). We then transform the raw DEM into iso-lines using the contour function built in QGIS, and we keep the line for which the elevation is equal to 20 m, providing us a delimiting line for the closed boundary (QGIS Development Team, 2024). The land area between the boundary and the coastline varies significantly. In areas where the coastline is steep, such as in the presence of cliffs, this land area tends to be much narrower. In areas with less steep coastline, the land area between the boundary and the coast tends to be larger. Reefs are represented inside (pink) and outside (lighter pink) the domain. The reefs are elements that will be used to parametrize a higher Manning coefficient and they are also used as refining points for the mesh. The domain is about 400 km long and 250 km wide.

The mesh is built using the `seamsh` python package, which is a python interface for the software GMSH developed at UCLouvain (Geuzaine and Remacle, 2009),

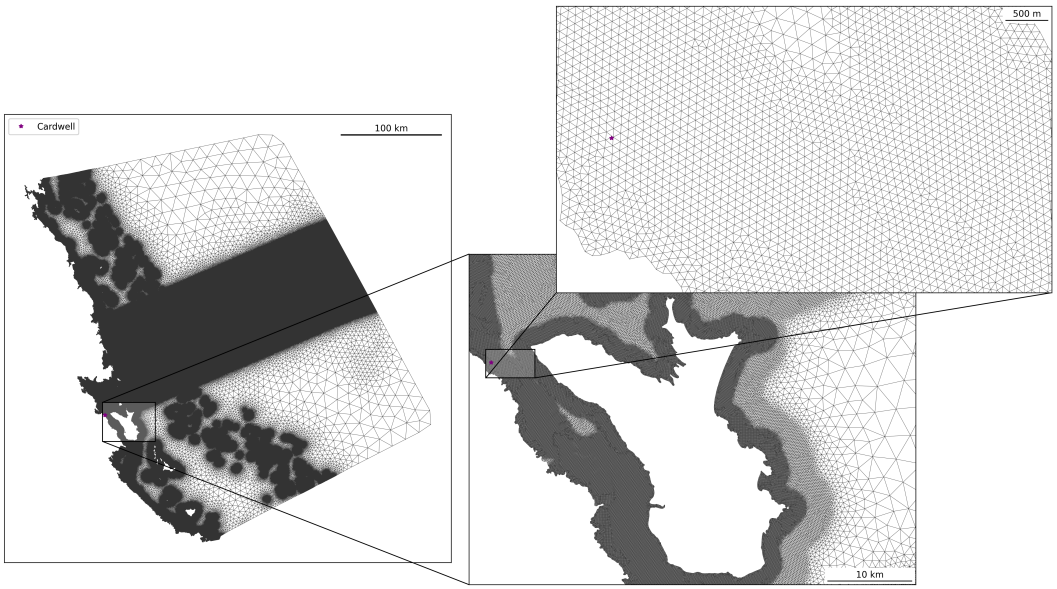

Figure 2.2: Main mesh used in most simulations, refined around the track, on land, near the coast and the reefs, 3 millions triangles, sizes ranging from 100 m to 15 km. The city of Cardwell is shown as the purple star.

by giving it a shapefile with domain boundaries tagged as "closed" or "open". The mesh is unstructured, which means it allows for different size of elements. This is very useful in our case, since we want a good resolution near the coast and on land, but we can allow a coarser resolution in the sea far from land (Legrand et al., 2006, 2007; Pietrzak et al., 2005).

When creating our mesh we refine it along three main components, the track of Yasi, the reefs and the coastal region, on land and in the sea near the land. For our main computations we will use one principal mesh, which is very fine, consisting of $3 \cdot 10^6$ triangles. Their nominal size ranges from 100 m near the coast, on land, around reefs, up until a distance of 3 km from these regions, then gradually scaling up to 15 km. Along the track, mesh elements have a minimal size of 250 m, in an area of 50 km around the track, then also scaling up to 15 km further away. This "base" mesh is shown in figure 2.2.

To answer our questions from the end of chapter 1, we also have a series of other meshes, that are coarser. We can observe these in figure 2.3. These meshes have a minimal element size of 2000 m (top left), 1000 m (top right), 500 m (bottom left) and 100 m (bottom right). They are all refined along the track except for the last one (bottom right), which is intentionally left unrefined to investigate whether such refinement is necessary.

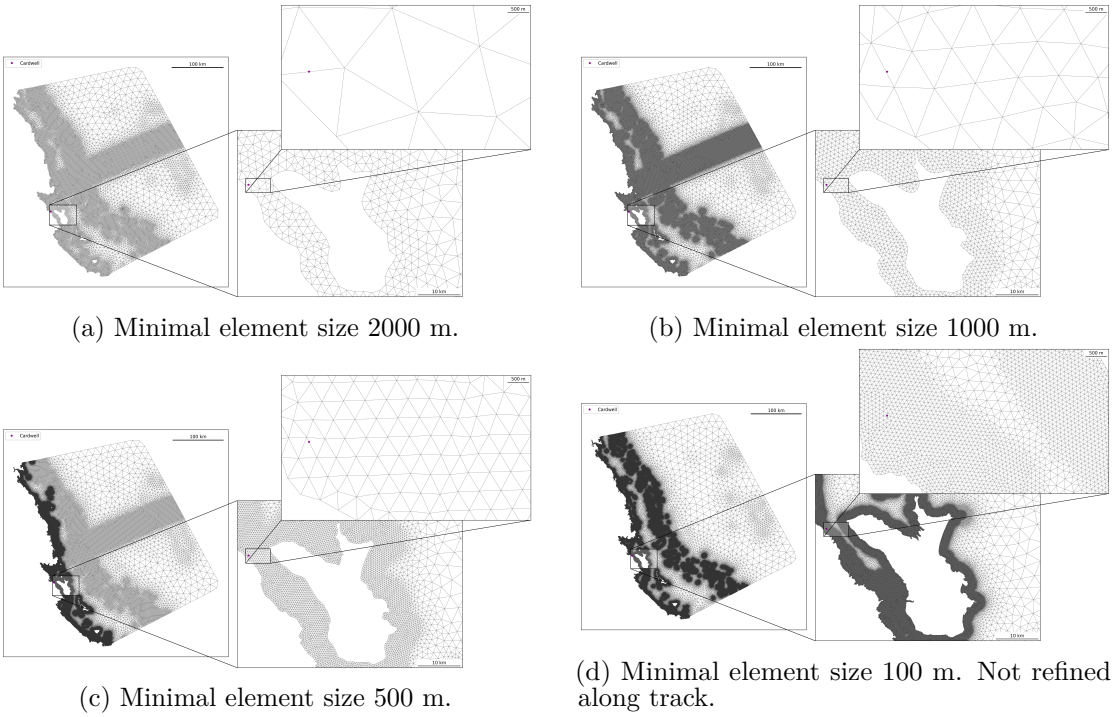

(a) Minimal element size 2000 m.

(b) Minimal element size 1000 m.

(c) Minimal element size 500 m.

(d) Minimal element size 100 m. Not refined along track.

Figure 2.3: Meshes with different minimal nominal sizes, domain is the same as in Figure 2.1.

The mesh size also rules the time steps for the computation, and thus has double impact on the computation time. Once because increasing the number of triangles increases the number of equations the computer solves, a second time because a smaller element requires a shorter time step. This is because we respect the Courant–Friedrichs–Lewy (CFL) condition for numerical analysis. It is a stability criterion used in numerical simulations to ensure that the time step (Δt) is small enough for the simulation to remain stable (Courant et al., 1967).

2.1.4 System inputs

In order to achieve accurate results, we rely on several important inputs, including bathymetry, tides and currents, and wind speed and atmospheric pressure. Each of these plays a key role in the quality of the simulations, which is why we selected data sources that provide the highest possible precision. The water depth is a particularly critical parameter, especially when dealing with shallow areas such as the Great Barrier Reef (GBR). There are two bathymetry sources that are suitable for our situation: the *General Bathymetric Chart of the Oceans* (GEBCO) database, a global database with a resolution of 15 arc seconds, approximately 440 m in Queensland, (GEBCO Bathymetric Compilation Group, 2024), and the *Deepreef* dataset described by Beaman, 2010, which is specific for Australia and has a resolution of 100 m. These two datasets are shown in Figure 2.4, we observe that they are similar. The colorbars are limited at -300 m and 100 m for visibility of the interesting data, the low coast and the shallow waters in the GBR. We need a closer look to show the differences near the coast, where the precision of bathymetry is the most important.

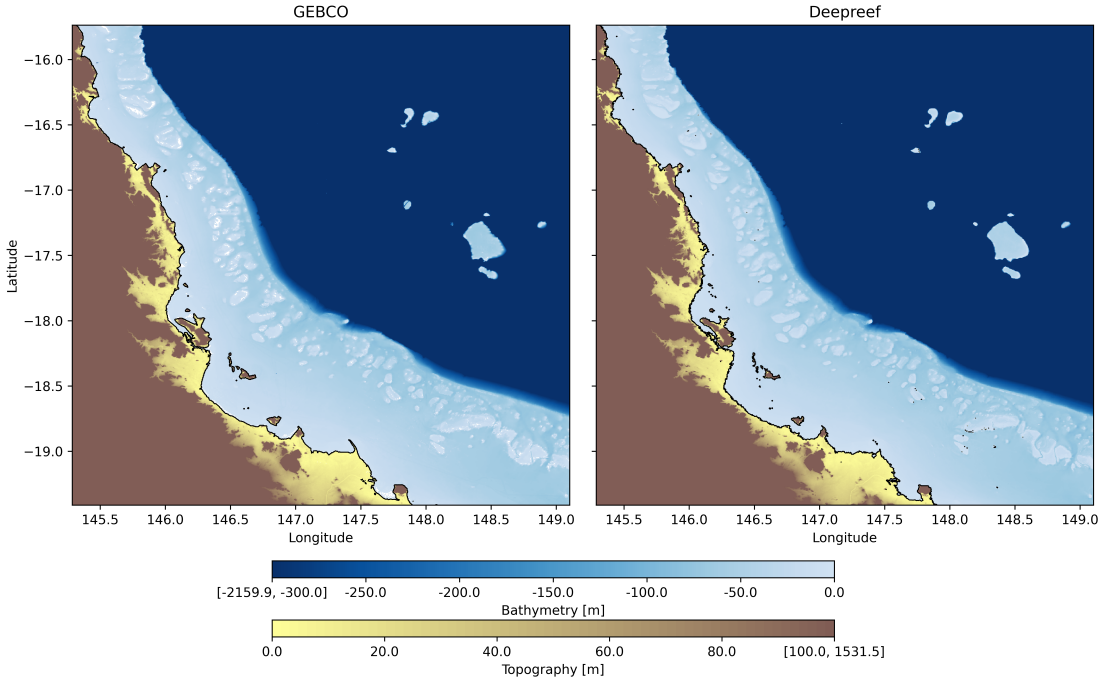

Figure 2.4: Bathymetry and topography from GEBCO (left) and Deepreef (right) in $[m]$. On the studied region, from $145.3°E$ to $149.1°E$ longitude and $19.4°S$ to $15.7°S$ latitude. Land is in yellow to brown shades and the sea in shades of blue.

In Figure 2.5, we see that the coast is smoothed when we look at GEBCO (left)

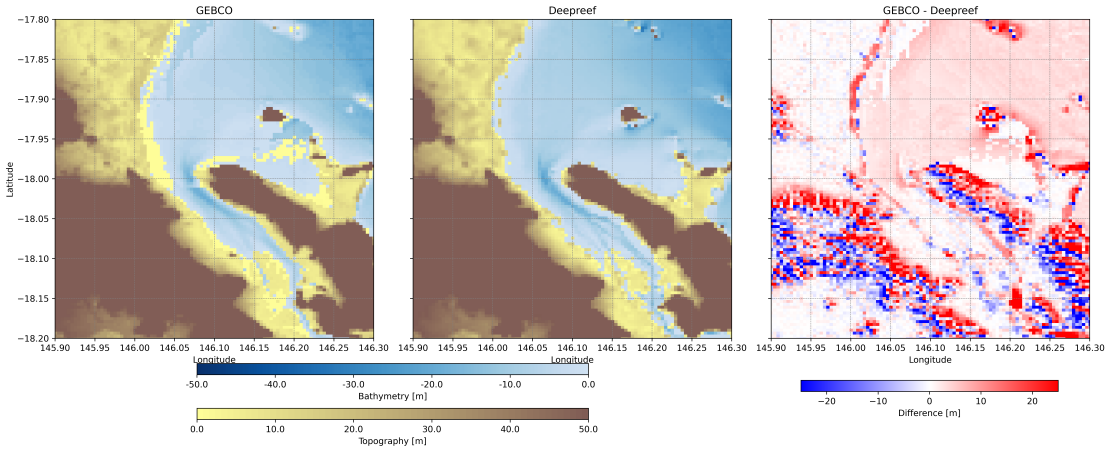

Figure 2.5: Close-up of bathymetry and topography from GEBCO (left) and Deepreef (middle) and the difference between both (right) in $[m]$ on coastal region near the city of Cardwell, from $145.9°E$ to $146.1°E$ longitude and $17.8°S$ to $18.0°S$ latitude. Land is in yellow to brown shades and the sea in shades of blue. The differences show a higher data from Deepreef in blue and a higher data from GEBCO in red.

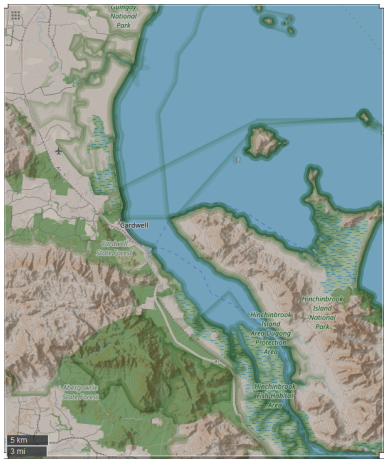

Figure 2.6: Map of the study area from $145.9°E$ to $146.1°E$ longitude and $17.8°S$ to $18.0°S$ latitude. From OpenStreetMap under the ODbL license, (OpenStreetMap Contributors, 2024).

data as opposed to Deepreef (middle). We also observe areas of inconsistency, such as a dry zone north of Hinchinbrook Island in the GEBCO dataset, that do not appear on other maps, such as OpenStreetMaps (OpenStreetMap Contributors, 2024) nor on the data from Deepreef (see Figure 2.6). On the right plot we show the bathymetry from GEBCO minus that of Deepreef, showing again that the differences lie in the coast which is the most important area in our case since it is the one becoming inundated. We can also see some differences in the higher altitudes, but this isn't relevant to our use of the data. Due to these inconsistencies and the generally coarser resolution of the GEBCO data, we chose Deepreef as source for

the bathymetry (and topography) throughout this project. The bathymetry we use is then projected on the mesh which reduces slightly the bathymetry quality. The bathymetry is smoothed to avoid large bathymetry gradients to enhance stability of the simulation.

On the open boundaries of our domain, we force the water elevation and currents. We retrieve these forcings from the Bluelink ReANalysis (BRAN) model from the Commonwealth Scientific and Industrial Research Organisation (CSIRO) (Chamberlain et al., 2021). These are provided daily with a spatial resolution of 0.1°, which equals 10 km. To reflect tidal variability and thus increase the accuracy of the model, we add tidal data from TPXO9 that has a spatial resolution of 1/30°, which is around 3.5 km in the latitudes of our domain (Egbert and Erofeeva, 2002).

As for the atmospheric data, the atmospheric pressure and the wind speed, which are the main drivers of storm surge, we employ the Era5 reanalysis data model (Hersbach et al., 2023). It is hourly and has a resolution of 0.25°, approximately 28 km in our latitudes. Another source for the wind speed is eReefs which provides the data with a better resolution, of 400 m (Steven et al., 2019). To grasp the precision of these models, we want to match the data they give to real-life measurements. Unfortunately, we don't have any wind speed and pressure measurement station near and active during the passage of cyclone Yasi. We thus need to widen the search region for stations. A good compromise of station location relative to cyclone track and data availability and quality is the measurement station of Lizard Island Relay Pole during the passage of Cyclone Ita in 2014 Australian Institute of Marine Science (AIMS), 2020. Ita was a tropical cyclone of category 5 that hit Queensland on the April 11, 2014, which had wind gusts up to 300 km/h (Australian Bureau of Meteorology (BoM), 2023). Figure 2.7 shows what the above mentioned models give during the passage of Cyclone Ita and the station measurements. For this we used a new domain, with the coast centered at the place Ita hit land. The meshing and domain properties are not important in this case as it is mainly used to show the different wind forcings.

In Figure 2.7 the pressure (top) is the same for eReefs and Era5, as eReefs doesn't provide atmospheric pressure information. The pressure in the models is not close to the actual observed pressure. The pressure drop is in reality much larger than what we have using the data models. Looking at the wind speed, we see that the observations (here "raw observations") have a high variability, the measurements where ranked "poor" during the cyclone hit on the station, April 11 at 11AM. However this still provides a good estimate of the conditions at that time. The wind speed from Era5 and eReefs are also quite far from the observations.

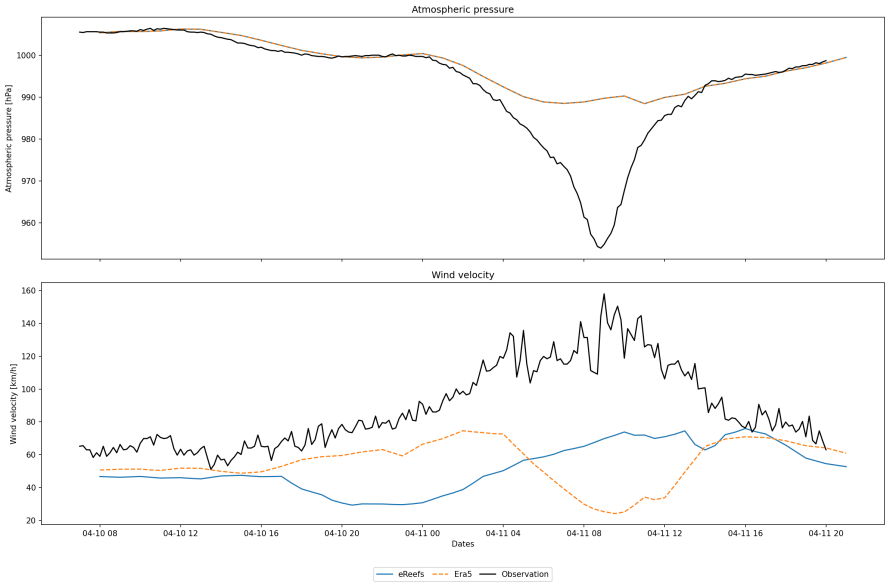

Figure 2.7: Atmospheric pressure (top) and wind speed (bottom) at the location of Lizard Island Relay Pole, coordinates $(14.691°S, 145.466°E)$. eReefs and Era5 data sets are in blue and yellow respectively, observations are in black.

Era5 even considers an intriguingly low wind speed when it is supposed to be at its peak according to measurements.

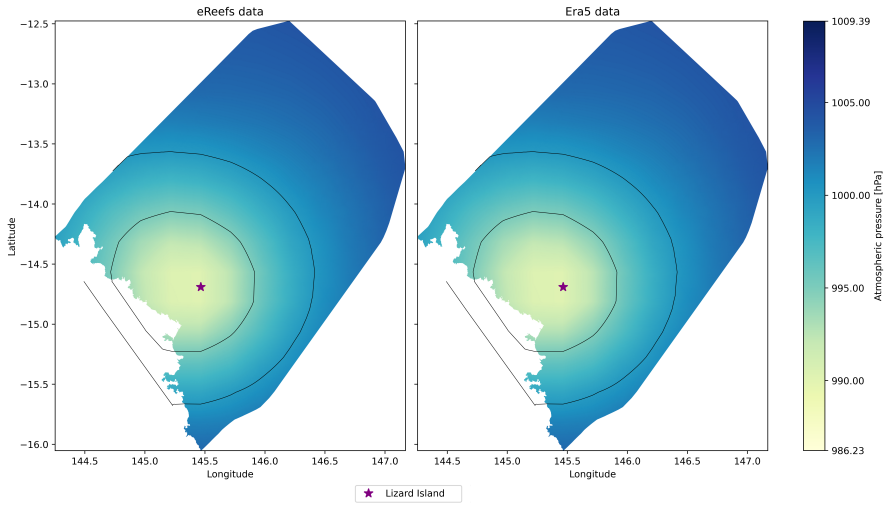

Figure 2.8: eReefs (left) and Era5 (right) data for atmospheric pressure over the domain in $[hPa]$, the location of Lizard Island Relay Pole, coordinates $(14.692°S, 145.466°E)$, is specified as the purple star, displayed data is of the 11/04/2014 at 11:00.

Figures 2.8 and 2.9 display the pressure and wind speed on the specially crafted

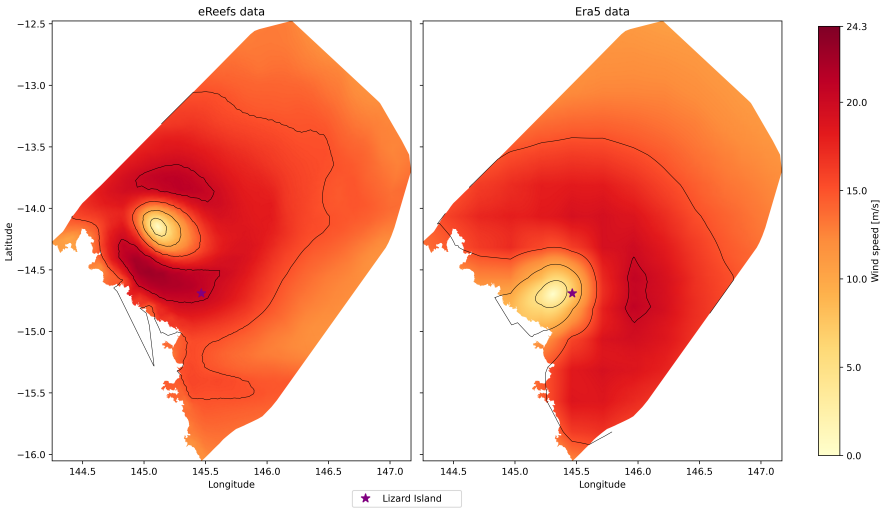

Figure 2.9: eReefs (left) and Era5 (right) data for wind speed over the domain in $[m/s]$, the location of Lizard Island Relay Pole, coordinates $(14.691°S, 145.466°E)$, is specified as the purple star, displayed data is of the 11/04/2014 at 11:00.

simulation domain for this cyclone for these two data sources at the time when the cyclone is closest to the Relay Pole (purple star on the map). We observe again the same profile for eReefs and Era5 as explained above. However the wind speed profiles look fairly different, they even locate the cyclone in different places. We cannot really rely on these data models on their own to capture the full strength, size and position of the cyclone. Since extreme conditions seem to be poorly captured by these models we introduce a specific model for cyclones to improve the quality of the wind forcings.

2.2 Holland's model and tropical cyclones

To improve the quality of the wind speed and atmospheric pressure forcings and thus of the simulation, we introduce a model for the pressure and wind profile of the cyclone. We chose Holland's model for tropical cyclones because of its simplicity, it only needs a few parameters and yet it is precise (Holland, 1980, Lin and Chavas, 2012). The only parameters it requires to compute the wind profile and the pressure profile are the position of the eye i.e. the track of the cyclone, the maximal wind speed of the cyclone, the radius of the cyclone for that speed, and the pressure drop in the eye of the cyclone. These are all given in two available databases that record cyclones (Australian Bureau of Meteorology (BoM), 2023 and Joint Typhoon Warning Center (JTWC), 2023).

2.2.1 Holland's model equations and validation

The model's wind profile equation reads, (Lin and Chavas, 2012):

$$V(r) = \left[\left(\frac{R_m}{r} \right)^B \frac{B\,\Delta P\, e^{\left[-\left(\frac{R_m}{r} \right)^B \right]}}{\rho} + \frac{r^2 f^2}{4} \right]^{\frac{1}{2}} - \frac{f\,r}{2} \tag{2.6}$$

$$\text{with } B = \frac{V_m^2 e\rho + f V_m R_m e\rho}{\Delta P} \tag{2.7}$$

with R_m, the Radius of maximum wind, ΔP, the pressure deficit in the cyclone's center, e, the base of natural logarithms, ρ, the density of the air, and f, the Coriolis parameter.

The pressure profile from the Holland's model reads:

$$p(r) = p_c + (p_n - p_c) e^{\left(\frac{-A}{r^B} \right)} \tag{2.8}$$

with A, a scalar parameter, p_c, the pressure in the eye, p_n, the ambient pressure taken at a long distance from the cyclone.

Using this model we can build new wind speed and atmospheric pressure profiles by combining them with Era5 for periods before, after, and for the parts of the domain that are far away from the cyclone track. We show these profiles and the base datasets in Figure 2.10.

The model also shows better profiles at the Lizard Island Relay Pole as shown in Figure 2.11. Looking at the pressure on the top graph, we observe the pressure found using the track record of JTWC (green) to be very close to the observations. We also observe a small drop in the red line (BOM). Overall in Figure 2.10 the track from BOM builds a smaller cyclone, thus explaining the smaller drop in the BOM line. On the lower graph of Figure 2.11 the wind speed using reconstructed models with track from BOM and JTWC are closer to the observations (in black). JTWC overshoots the observations while BOM tends to undershoot them slightly. However, as mentioned, the observations are not perfect as the measurement conditions are rather extreme. If the measurements are ranked as poor, it is likely because the wind was too strong for the station's capacity, potentially indicating stronger winds than those recorded. In reality, the actual wind speeds during the peak could be either higher or lower than the measured values.

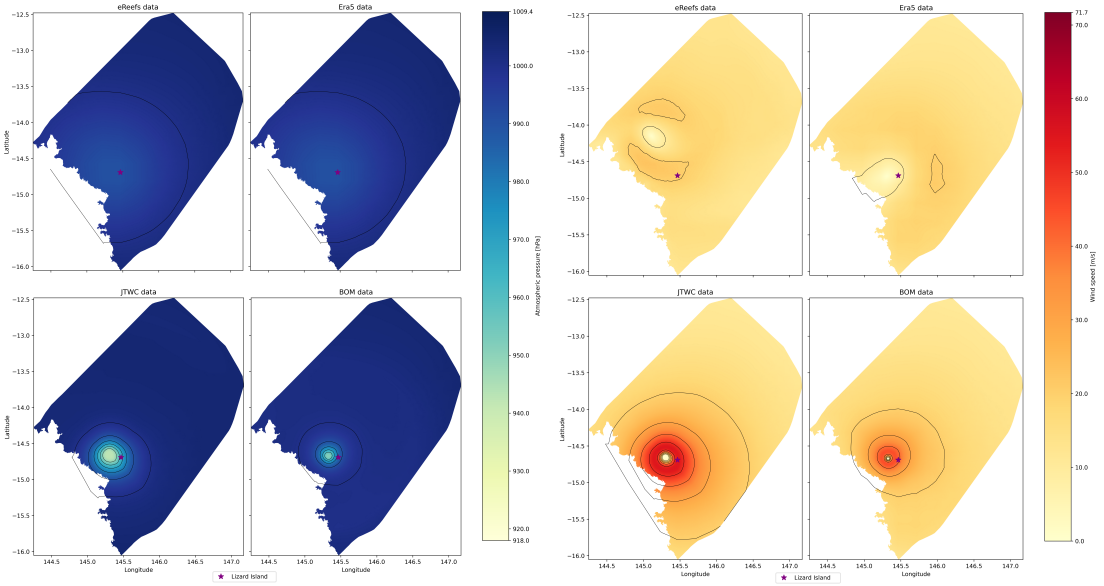

(a) Atmospheric pressure in $[hPa]$. (b) Wind speed in $[m/s]$.

Figure 2.10: Atmospheric pressure (a) and wind speed (b), using data from eReefs (top left), Era5 (top right) and Holland models using JTWC track data (bottom left) and BOM track data (bottom right). The location of Lizard Island Relay Pole, coordinates $(14.691°S, 145.466°E)$, is specified as the purple star, displayed data is of the 11/04/2014 at 1100.

These cyclone models are provide good estimates, especially when comparing to the two data sources we had initially, eReefs and Era5. As shown in Figure 2.10, the cyclones are barely visible in the top row when using the colorbar that is adjusted to the reconstructed profiles in the bottom row.

This said about Holland's model we can set the domain for cyclone Ita aside, as it served only to validate Holland's model due to the wind measurement data unavailability for cyclone Yasi. This validation allows us to showcase the importance of Holland's model in such scenarios.

2.2.2 Wind drag parametrization

It is important to note that when the wind reaches a high velocity, the water surface becomes turbulent and air mixes with the water, forming small air and water droplets. When the wind reaches a certain point a white "foam" called spume appears. This induces a drag saturation since the water underneath is separated from the wind by this layer (Powell et al., 2003, Liu et al., 2012, Moon et al., 2004 and Moon et al., 2007). The model used for the drag parametrization is as

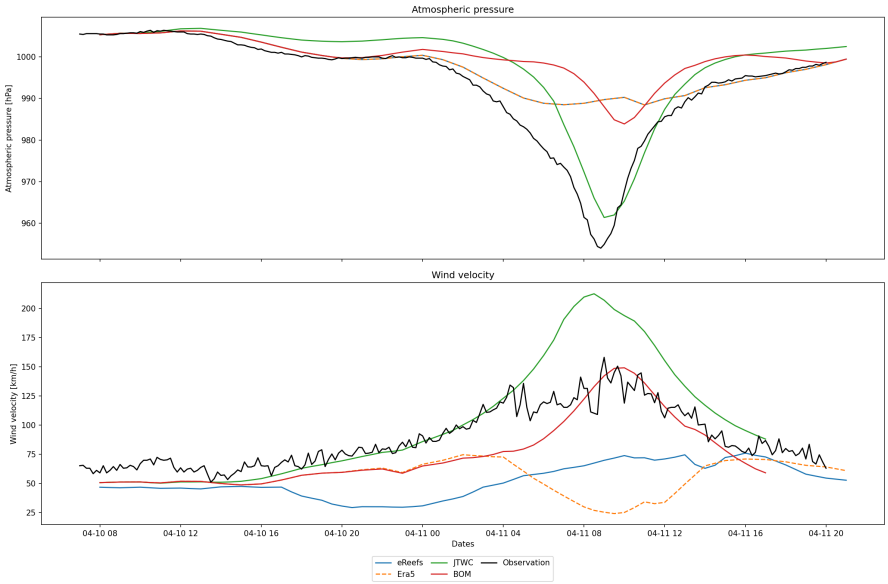

Figure 2.11: Atmospheric pressure (top) and wind speed (bottom) at the location of Lizard Island Relay Pole, coordinates $(14.691°S, 145.466°E)$. eReefs, Era5 and observations data data are in blue, yellow and black respectively, reconstructed data using Holland's model with JTWC and BOM track data are in green and red.

described in Dobbelaere et al., 2022. The drag coefficient C_d reads:

$$C_d = \kappa^2 \log\left(\frac{10}{z_0}\right)^{-2} \tag{2.9}$$

with κ, the von Karman constant, U_{10} the wind speed at 10 m over sea level, and z_0 is the roughness length given by:

$$z_0 = \begin{cases} \frac{0.0185}{g} u_*^2, & \text{if } U_{10} \leq 12.5\,\text{m/s}, \\ [0.085\,(-0.56u_*^2 + 20.255u_* + 2.458) - 0.58] \times 10^{-3}, & \text{if } U_{10} > 12.5\,\text{m/s}. \end{cases} \tag{2.10}$$

In this last equation, u_* is the friction velocity, it bounds the wind speed and the ocean dynamics and is given by:

$$U_{10} = -0.56u_*^2 + 20.255u_* + 2.458. \tag{2.11}$$

2.2.3 Cyclone Yasi

We now consider cyclone Yasi again and the domain described in section 2.1.3. Using the track data from BOM and JTWC, we obtain the following profiles.

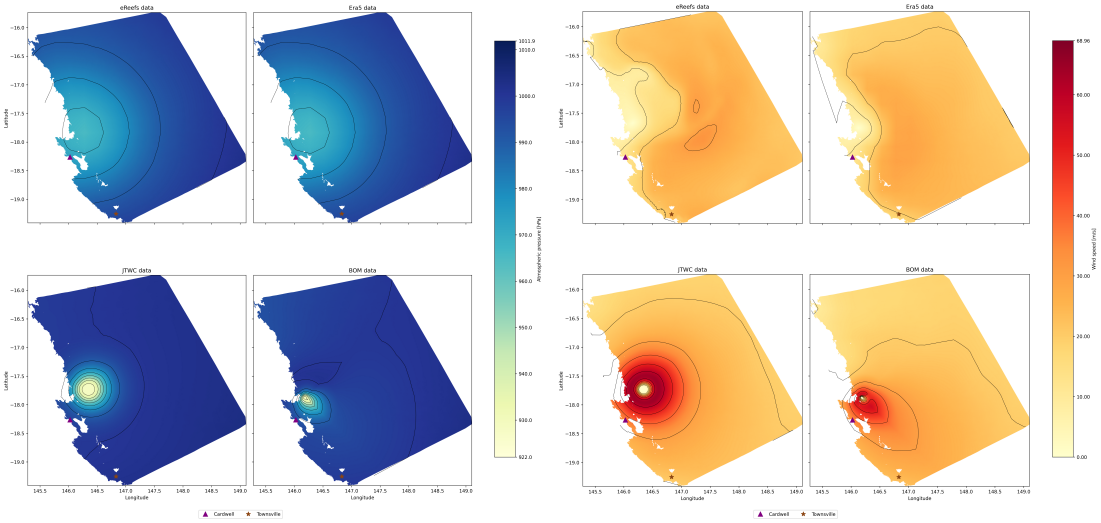

(a) Atmospheric pressure in $[hPa]$. (b) Wind speed in $[m/s]$.

Figure 2.12: eReefs (top left), Era5 (top right) and Holland models using JTWC track data (bottom left) and BOM track data (bottom right) data for atmospheric pressure (a) and wind speed (b), on the domain for the case Yasi. Two storm surge monitoring sites are shown, the city of Cardwell as the purple triangle and the brown star for the city of Townsville. Displayed data is of the 02/02/2011 at 14:00.

The pressure (Figure 2.12a) also shows a stronger and larger drop with JTWC (bottom left) than with BOM (bottom right) track data, while both still show stronger pressure drops than the basic data model Era5. This is also the case for the wind in Figure 2.12b. Overall we observe that the track data from JTWC produces a larger and more severe cyclone, with the wind speed reaching 68.96 m/s. Whereas with track data from BOM, the maximal wind speed is 56.46 m/s. The pressure drop is also greater when using the track data from JTWC, for which the pressure minima is 922 hPa, while it is 929 hPa for BOM. These extremas are recorded on the entirety of the cyclone's life, in order to watch all snapshots with the same colorbars. Black lines are iso-lines corresponding to the ticks of the colorbar.

Figure 2.13 and 2.14 depicts a snapshot of Yasi's atmospheric pressure's (left) and wind speed's (right) reconstructed profiles using Holland's model with track data from JTWC and from BOM respectively. We see the strong pressure drop (yellow) and the high wind speeds (red), and again the cyclone is larger with the track from JTWC. The track and Saffir-Simpson scale are added to the figures (Taylor et al., 2010) to increase readability of the path. The JTWC classified Yasi as a category 5 TC, while the Australian Bureau of Meteorology classified it as a category 4 cyclone. We also added small quivers to the wind speed figures to

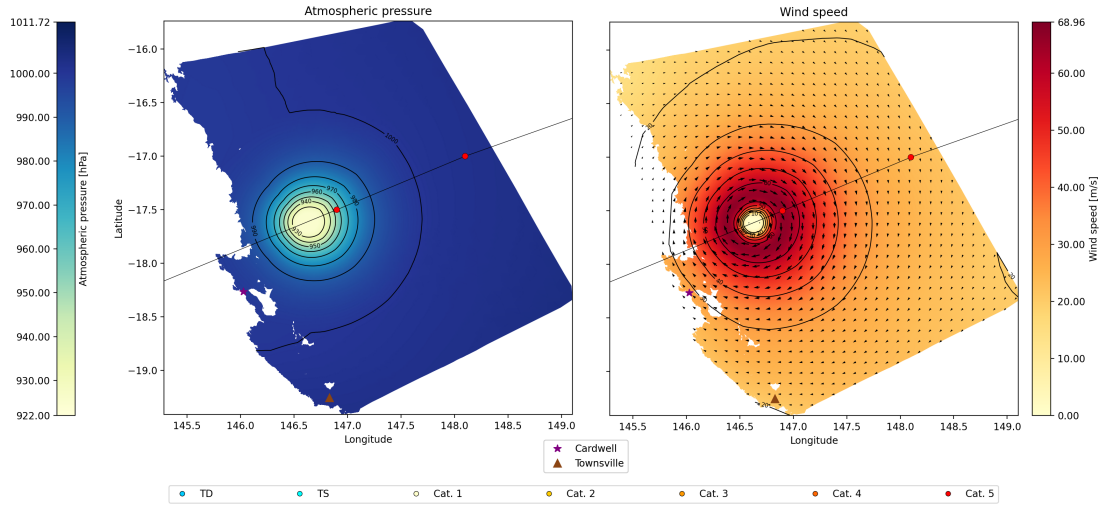

Figure 2.13: Snapshot of atmospheric pressure (left) and wind speed (right) using a reconstructed Holland's model with track data from JTWC. Time of snapshot is 2011/02/02 13:00.

visualize their direction. The cities of Cardwell and Townsville are shown as the purple star and brown triangle. Cardwell is located right in the path of the cyclone.

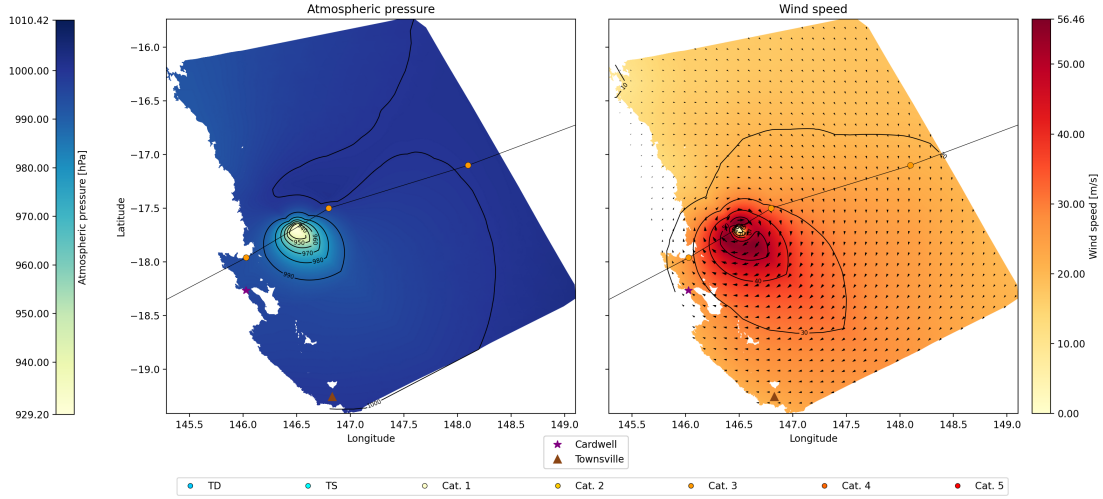

Figure 2.14: Snapshot of atmospheric pressure and wind speed using a reconstructed Holland's model with track data from BOM. Time of snapshot is 2011/02/02 13:00.

Chapter 3

Results

In this chapter, we first cover the validation of the hydrodynamic model to demonstrate its applicability. Afterwards we present the results obtained concerning the flooded area, the mesh size sensitivity of these results, and the interaction between tides and a cyclone storm surge. The results are based on simulations conducted from January 25, 2011, to February 5, 2011. This time frame allows the model to use the period between January 25 and the cyclone's arrival within the domain as a buildup phase.

3.1 Result validation

We first want to show the model's simulated surge compared to real life measurements. There are a few storm surge monitoring sites that are inside our simulation domain and that are active during Cyclone Yasi's landfall on February 2, 2011.

The monitoring sites are installed by the government of Queensland and provide a measurement of the water height every ten minutes at different locations that can be seen in Figure 3.1 as the red dots, with their name attached (Queensland Government, 2011, 2015). Near the cyclone path we have three sites, Mourilyan, Clump Point and Cardwell. Further away from the cyclone, around 200 km south we have a fourth site in the city of Townsville.

The results of the simulations, using the four different wind forcing sources we described at the end of section 2.2 are shown in Figure 3.2. First we can observe Figures 3.2 and 3.3b. We see that outside of the period where the cyclone arrives on the coast, (between the red dotted lines) the Root Mean Square Error (RMSE) is low and the simulations follow closely the observations. It is important to note that the simulations' water level is not the same as the level depicted in

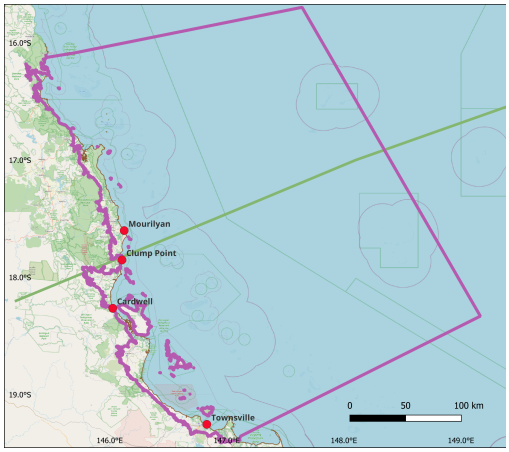

Figure 3.1: Map of central Queensland, with the domain borders in purple, the track of Yasi using data from JTWC in green, and the validation points in red (OpenStreetMap Contributors, 2024)

the figure. The bathymetry is smoothed in the simulation and not the same as the bathymetry the observation measurements consider. To compensate visually for this we raised artificially the simulation lines in the figures to fit the beginning of the observation lines. This raised line, is the one used for RMSE computation. This lack in bathymetry exactitude is also behind the fact that the simulations do not reach the bottom for some of the low tides, as can be seen on the Cardwell, Townsville and Mourilyan plots (Figure 3.2). During low tides at these points, the simulations show a water level of $H_{lim} = 0.01\,[m]$ which is the minimal water level for wetting and drying. This of course impacts negatively the RMSE.

Focusing on the cyclone period, we can divide the set of points in two classes, those who measured in real life a substantial surge during the cyclone's passage, Cardwell and Clump Point, and the other two points not showing a special surge, Townsville and Mourilyan. Townsville, being far from the cyclone, shows a lower surge. Although we still observe a prolonged high tide and higher low tide than we could expect from seeing the previous tide cycles. For the second point in this category, Mourilyan, which is close to the track of the cyclone, we could have expected a higher surge than what is measured. But we still have a tide that is higher than what the regular tide cycle predicts by 1 m.

For the points with a visible surge in the observations, we observe on the left column of both Figures 3.3b and 3.3a that the simulation that is closest to observation is the one using a reconstructed cyclone model with track data from JTWC (red lines in Figures 3.2 and 3.3a). The simulation using data from BOM performs somewhat poorer than the simulation using data from JTWC in Cardwell, and is very close to the simulations using basic data models Era5 and eReefs in

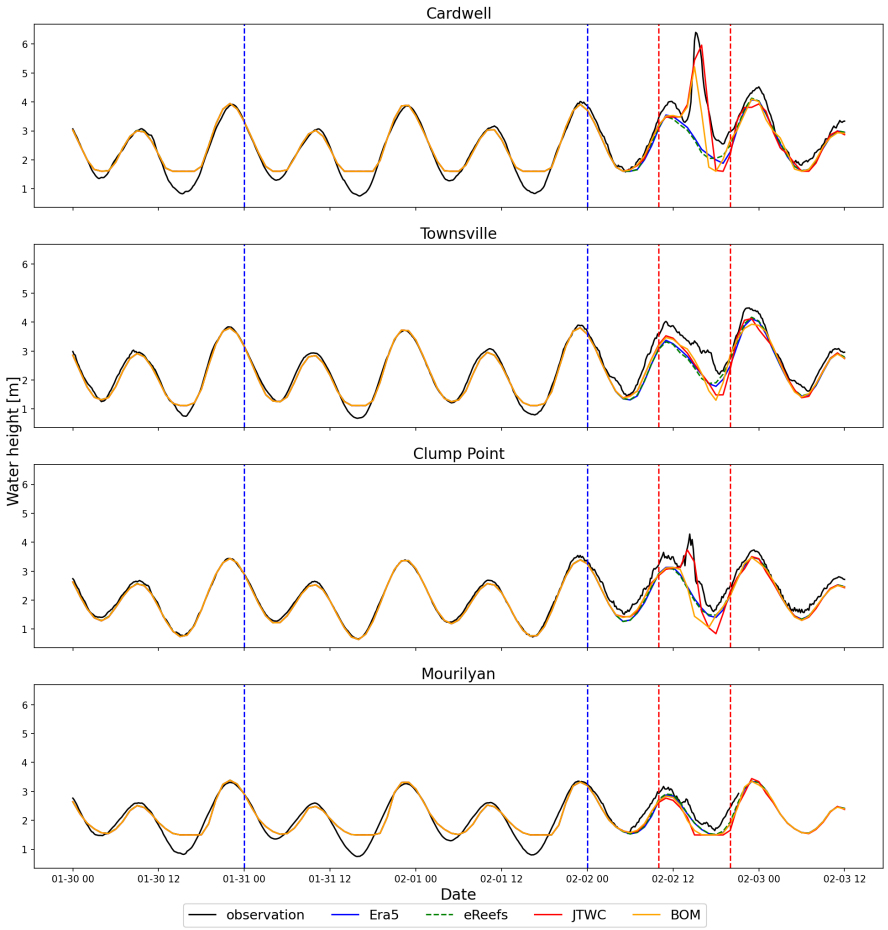

Figure 3.2: Water elevation in $[m]$ at the location of the different validation points. Observation of the said site is in black. Simulations results using data from Era5, eReefs, JTWC and BOM are in blue, green, red and yellow, respectively. Blue dotted vertical lines denote the time period for "regular" Root Mean Square Error (RMSE) computation, red vertical lines delimitate the time period used for computation of RMSE during cyclone passage.

Clump Point. The highest surge recorded by observation is in Cardwell and the simulation using JTWC track data is off by around 40 cm where the simulation using BOM data is lacking more than a meter. Using JTWC data is also the setup that has the lowest mean RMSE across all validation points.

3.2 Cyclone model and inundations

In this section we present maps of the maximal water height for each element throughout the simulation (inundation maps), highlighting areas that were sub-

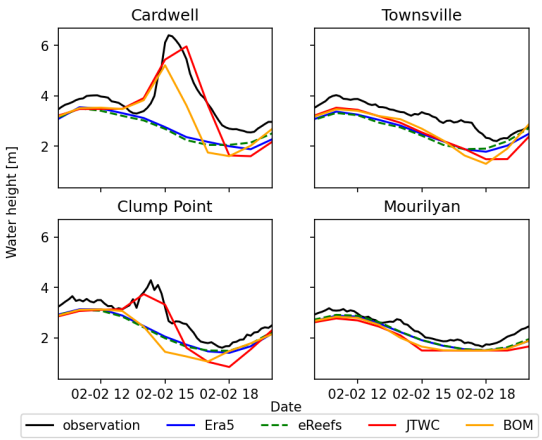

(a) Close-up of Figure 3.2 during cyclone period (red dotted lines), results of the simulations using wind forcings from Era5, eReefs, JTWC and BOM in blue, green, red and yellow respectively.

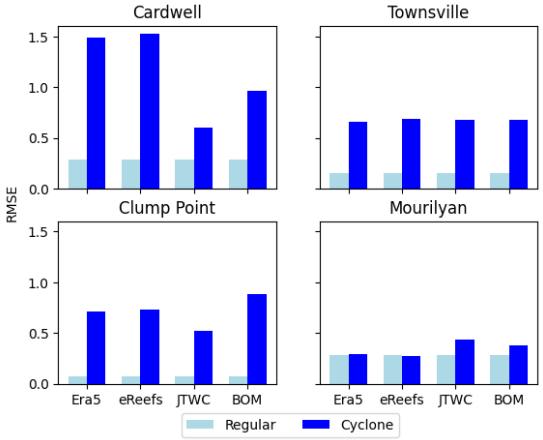

(b) RMSE between observation and simulations, RMSE for regular period in light blue (between blue lines in Figure 3.2) and in darker blue for the time period when the cyclone hits land.

Figure 3.3: Close-up of Figure 3.2 (left) and RMSE for each of the simulations with relation to observations, for both time periods described in Figure 3.2 (right).

merged at least once during the cyclone's landfall. For visibility purposes, the maps are zoomed in on selected validation points. We begin with a close-up of Cardwell, followed by the inundations around the Mourilyan point situated close to the TC track. We also take a look at the flooding near the city of Innisfail, north of the Mourilyan point and the region around Clump Point.

In Figure 3.4, we observe again that the cyclone model that simulates the larger inundation is the Holland's model with JTWC track data (bottom left); the surge is higher at the coast, and the inundation reaches further inland. The simulation conducted using BOM track data (bottom right) and the simulation with JTWC data share some areas that are submerged. However the simulation using track data from JTWC goes deeper inland in those areas. This difference is especially visible in the lower part of the map, where we have a very large zone that is flooded, but that also has a high water level when flooded. There is little to no flooding when using wind forcings from Era5 and eReefs, except for areas usually submerged during a high tide. We now focus on the results for simulations using Holland's model for wind speed and atmospheric pressure with track data from JTWC.

Zooming in on the city of Cardwell, we can compare this to a mapping of the population density in Figure 3.5c. Here we use a map of hexagons from Kontur, with each hexagon having a surface of 0.76 km^2 (Kontur, 2023). This simulation

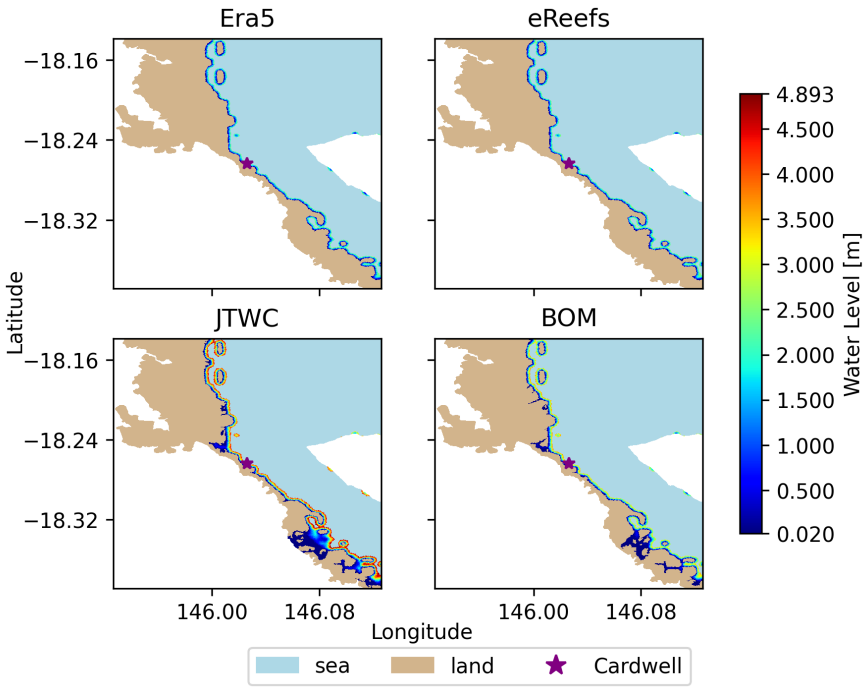

Figure 3.4: Inundation map of the region around Cardwell with simulations using wind forcings from Era5 (top left), eReefs (top right), JTWC (bottom left) and BOM (bottom right). Dry land and the sea are in tan and light blue respectively, submerged land zones' water height are ranging from 2 cm to 4.893 m and are displayed with the colorbar on the right. White is outside of the simulation domain. The Cardwell storm surge monitoring site is the purple star.

shows that the cyclone has flooded regions in Cardwell where 539 people live. This number is calculated by taking the number of people in a hexagon if the center of this hexagon is submerged. We can also compare the cyclone inundation to a normal high tide, in Figure 3.5b. We observe a clear difference, both in the flooded areas and in the water level near the coast. The submerged area on the map is 32.04 km^2, whereas when computing areas for the Era5, eReefs and BOM simulations, we have a submerged area of 16.36 km^2, 16.69 km^2 and 25.95 km^2 respectively.

We now look at Figure 3.6 of the simulation results zooming in on the region around the validation point Mourilyan. Again we observe the flooding with the cyclone (left), and a normal tide (center). The map shows a submerged region of 21.37 km^2 and the population impacted by the cyclone is 179 persons, using population data from Kontur, shown in Figure 3.6c. We can notice that the flooding joins a river and a small lake in the middle of the figure, and that there is a lake that floods its surroundings in the first third of the figure from the top.

In Figure 3.7 we observe the simulation results around the city of Innisfail

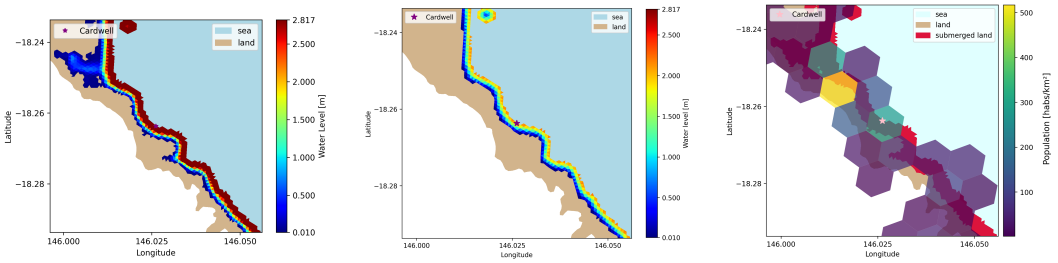

(a) Enlarged view of Cardwell from Figure 3.4 using wind forcings from JTWC.

(b) Snapshot of simulation results using JTWC data at high tide without the cyclone.

(c) Population concentration map, with inundated areas (red) from Figure 3.5a.

Figure 3.5: Close-up of the city of Cardwell. Inundations summary (left), water level during a normal high tide (center) and population concentration (right).

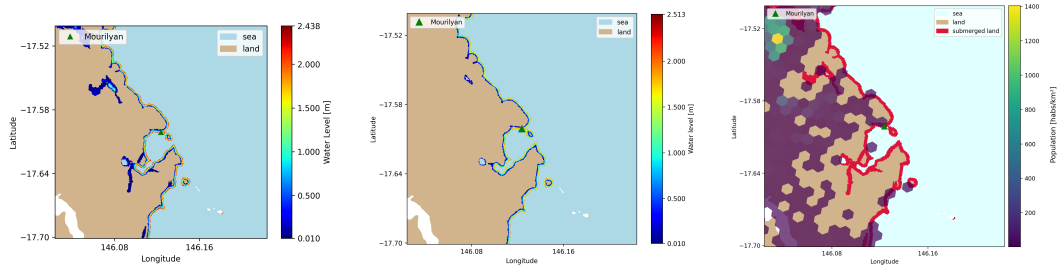

(a) Flooding map around Mourilyan point, simulation results, wind data from JTWC.

(b) Snapshot of simulation results at high tide before the cyclone.

(c) Population concentration map, with inundated areas (red) from Figure 3.6a.

Figure 3.6: Close-up of the region around validation point Mourilyan, inundations summary (left), water level during a normal high tide (center) and population concentration (right).

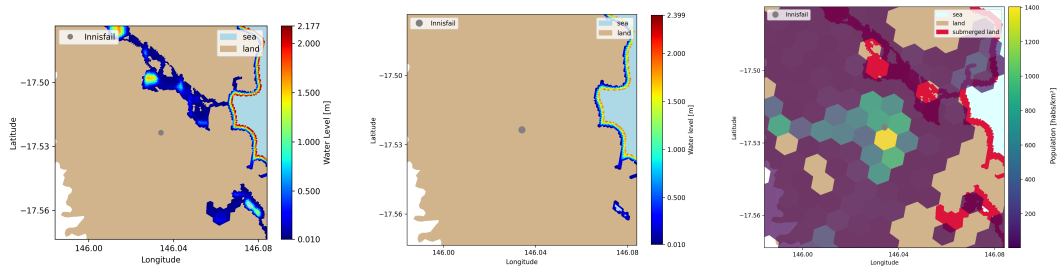

(a) Flooding map around Innisfail city, simulation results with wind data from JTWC.

(b) Snapshot of simulation results at high tide before the cyclone.

(c) Population concentration map, with inundated areas (red) from Figure 3.7a.

Figure 3.7: Enlarged view of the city of Innisfail and surroundings, located just north of the Mourilyan validation point, inundations summary (left), water level during a normal high tide (center) and population concentration (right).

centered in the gray dot, located about 10 km north of the Mourilyan validation point, near the coast. The simulation does not show flooding in the most populated

regions, however in the areas surrounding the city the results show a flooding of an area of 12.08 km^2 where there are 244 inhabitants.

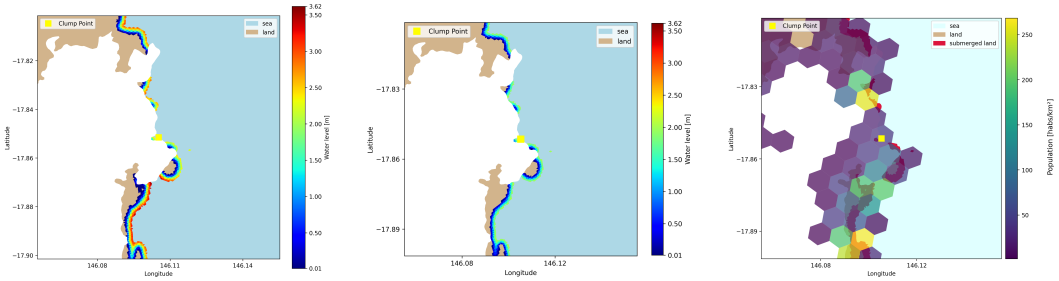

(a) Flooding map around Clump Point, simulation results with wind from JTWC.

(b) Snapshot of simulation results at high tide before the cyclone.

(c) Population concentration map, with inundated areas (red) from Figure 3.8a.

Figure 3.8: Enlarged view of the region around validation point Clump Point (yellow square), inundations summary (left), water level during a normal high tide (center) and population concentration (right).

In Figure 3.8, showing Clump Point, the outside of the domain (white area) is very near to the coast. Sometimes there is even no visible coast, as seen just north of the validation point (yellow square). This is because the coast is very steep and is above 20 m very close to the water. Due to this, we will not include maps of this point further on. However we will still use the storm surge measurements from this validation point. On this map the flooded region has an area of 35.5 km^2 and the flooding impacts 353 people.

We summarize the results for each of the locations in Figure 3.9. Figure 3.10 summarizes the total submerged area (blue) and affected population (red) for the entire domain.

Each graph in Figure 3.9 focuses on the region around the point or city. Clump point (top left) area and Innisfail (top right) area are as presented in figure 3.8 and 3.7, they both cover about 12 km coastline. We kept the larger view of the Cardwell area (middle left) from Figure 3.4 which covers 28 km of coast, and the smaller zoomed in area from figure 3.5a covering about 7 km of coast (middle right). We also include an area around the city Townsville (bottom left) which covers 20 km of coast and Mourilyan (bottom right) is as presented in figure 3.6 also covers about 20 km of coast.

In Figure 3.9 we again observe that the simulation using track data from JTWC is the one with the most inundated surface area and with the largest impacted

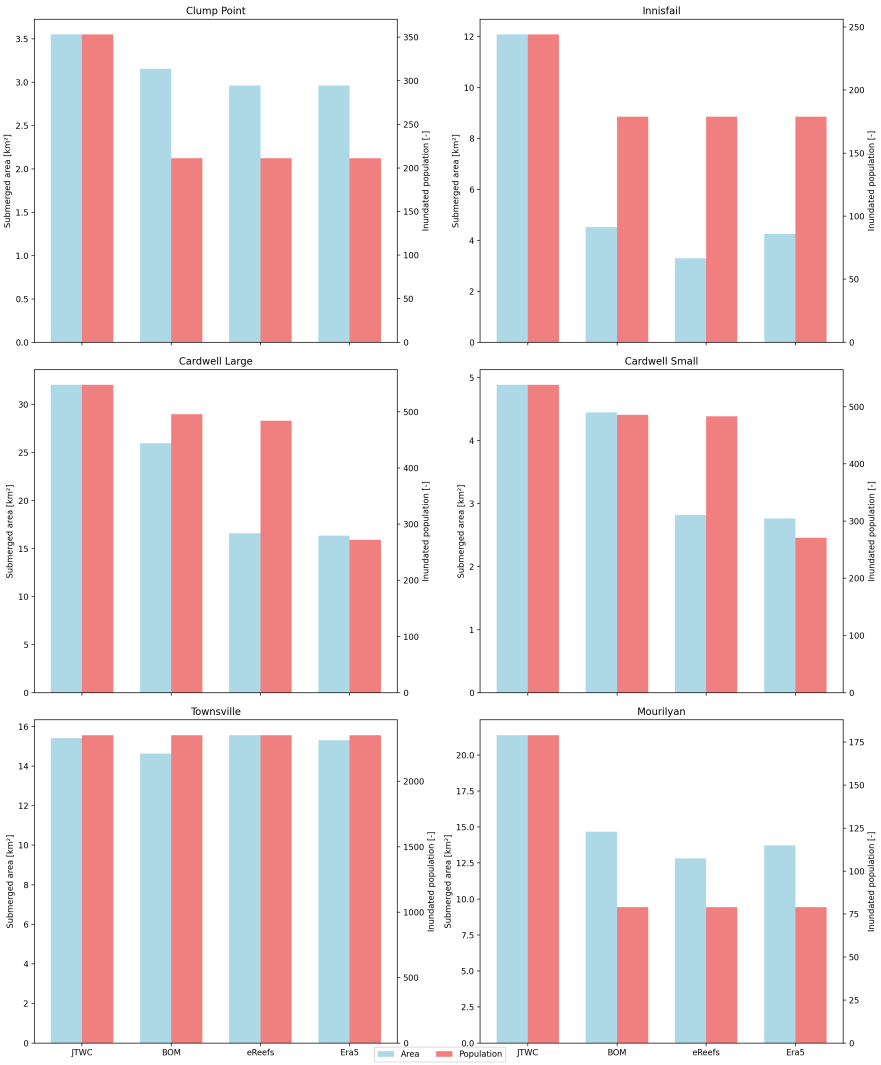

Figure 3.9: Summary of the results of the simulations for each zone of interest. The x-axis represents the wind forcing sources, from left to right, JTWC, BOM, eReefs and Era5. Submerged area is in blue and the impacted population is in red.

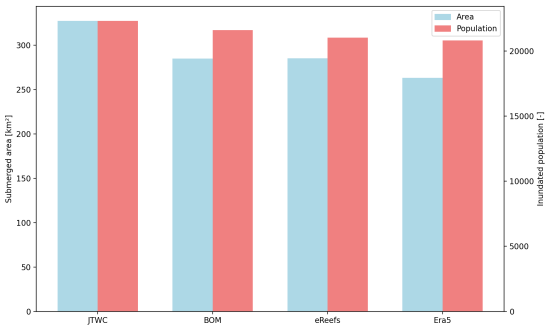

Figure 3.10: Summary of the results of the simulations over the entire domain. The x-axis represents the wind forcing sources from left to right, JTWC, BOM, eReefs and Era5. Submerged area is in blue and the impacted population in red.

population. Between "Cardwell Large" (middle left) and "Cardwell Small" (middle right) the population that is impacted is roughly the same size, as most people in that area live in or close to the city, while the area that is submerged is significantly reduced since the considered zone is much smaller. For Townsville the different simulations results show insignificant inundation, the population impacted is roughly the same for all simulations in that area. Again, we can see in the last figure of this section, which summarizes the results for the entire domain, that we have a larger submerged area (blue) and a larger population impacted by the surge when using track data from JTWC.

3.3 Effects of the mesh resolution on results

In this section, we show results for different simulations all using wind forcings from the reconstructed model explained in section 2.1.3 with track data from JTWC. The simulations each has a different mesh and thus mesh resolution. We want to show the effect on the result's precision by the refinement of the mesh. We first look at the results and compare them to validation data such as in the previous section. Then we look at the inundations maps and the submerged areas and impacted population.

3.3.1 Validation of simulations with different mesh resolution

The meshes used in the different simulations for this section are described in section 2.1.3. We use the four meshes that are refined along the coast, on land, on and around the reefs and following the track of tropical cyclone Yasi. We refer to them by the size of their smallest element: mesh 100, mesh 500, mesh 1000 and mesh 2000.

In Figure 3.11, we observe the water elevation in the storm surge validation points. We first see that we only have results for Clump Point with the base mesh, mesh 100, as this point is outside of the coarser meshes due to smoothing of the boundary.

Then we observe the large difference between the simulation using mesh 500 (green) and the observations (black) in the Cardwell and Mourilyan sites. This difference comes from the bathymetry projection on the mesh. The bathymetry differs significantly between the different meshes as shown in 3.1. We do not have the same interpolation of the bathymetry on each mesh, and the smoothing also differs as it is resolution dependent. This implies large variations when looking at results in the validation points.

We observe also that the coarsest mesh, mesh 2000, (yellow line) shows a lag compared to the tidal cycle in Cardwell and Townsville. In Townsville, the bathymetry is 85 cm higher than that of the mesh 100 explaining the high lows of the tide. However, in Cardwell the bathymetry is close to the one of the base mesh (mesh 100) and still shows the lag. At the same time, mesh 500 and mesh 1000 in Townsville show a blocked low tide, but still follow the observation closely during the high tide.

In Figure 3.12 we explore more in depth the period when Yasi hits land and show the RMSE between observation and simulation results. We have, as for the

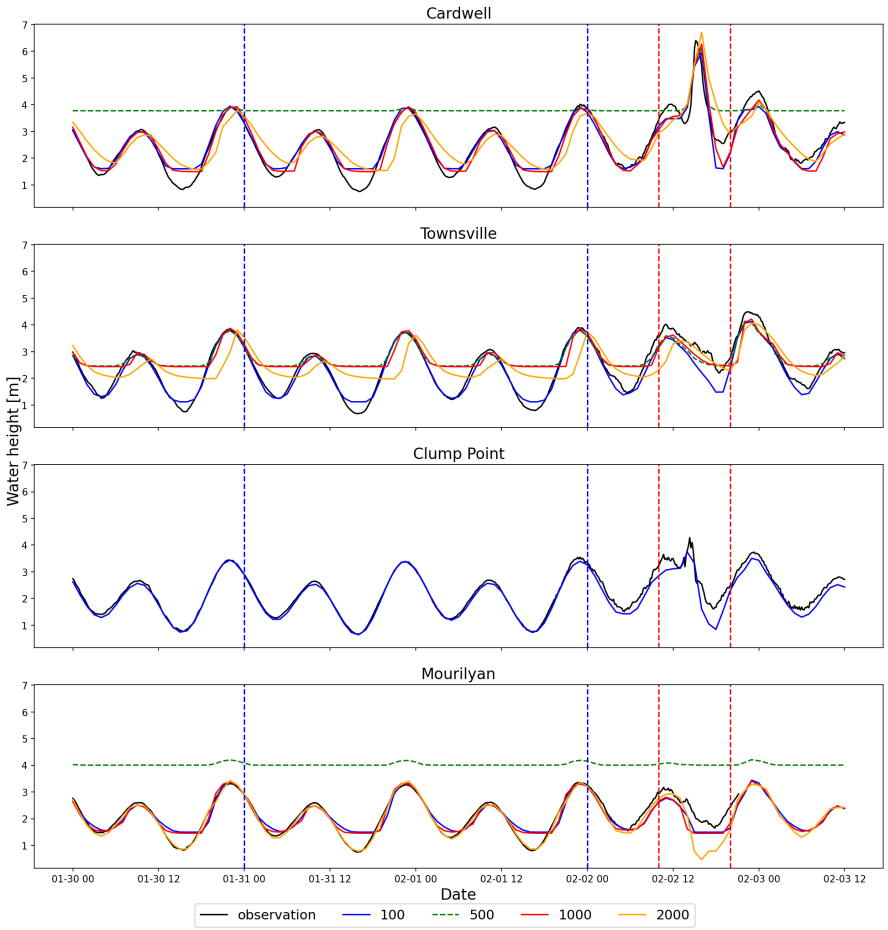

Figure 3.11: Water elevation in $[m]$ at the location of the different validation points. Observation of the said site is in black. Simulations results using meshes with smallest element of size 100, 500, 1000 and 2000 are in blue, green, red and yellow, respectively. Blue dotted vertical lines denote the time period for RMSE computation, red vertical lines delimitate the time period used for computation of RMSE during cyclone passage.

previous section, two different RMSE, the first (regular) is computed for a time period before the cyclone interacts with the coast (between the blue dotted lines in Figure 3.11), the second (cyclone) is the RMSE during the period the site is impacted by the cyclone (in between the red dotted lines).

In this figure we also see that as a general tendency, the RMSE grows with the mesh size. However it is not the case for each validation point. Especially in Townsville during cyclone landfall, the coarser meshes provide a solution close to observation, even better than the "base case" (in blue). However the difference isn't very large and occurs when the water level descends. The regular RMSE is strongly influenced by the refinement of the mesh, and the bathymetry at the point.

Mesh	Cardwell	Townsville	Clump Point	Mourilyan
Mesh 100	$-0.06\ [m]$	$0.28\ [m]$	$1.59\ [m]$	$-0.24\ [m]$
Mesh 500	$-2.23\ [m]$	$-1.06\ [m]$	/	$-2.75\ [m]$
Mesh 1000	$0.05\ [m]$	$-1.04\ [m]$	/	$-0.20\ [m]$
Mesh 2000	$0.03\ [m]$	$-0.57\ [m]$	/	$0.84\ [m]$

Table 3.1: Table of bathymetry in $[m]$ at validation points for each mesh, negative values imply the point is on land.

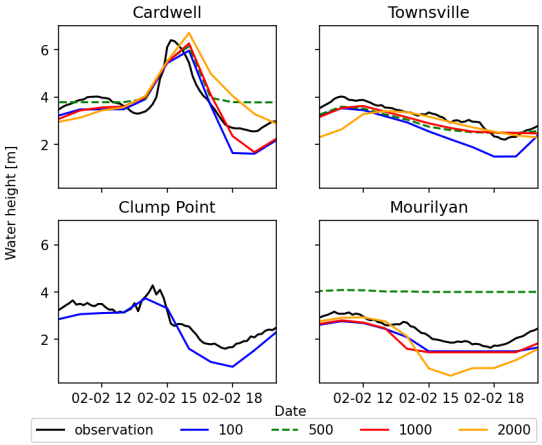

(a) Close-up of Figure 3.11 during cyclone period (red dotted lines), results of the simulations using meshes 100, 500, 1000 and 2000 in blue, green, red and yellow respectively.

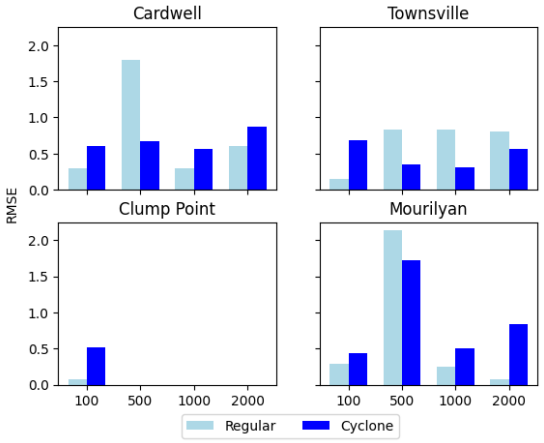

(b) RMSE between observation and simulations, RMSE for regular period (in blue in Figure 3.11) in light blue and in darker blue for the landfall period.

Figure 3.12: Extract of Figure 3.11 (left) and RMSE for each of the simulations with relation to observations, for both time periods described in 3.11 (right).

The cyclone RMSE on the other hand is more complicated to characterize. It stays relatively low when the mesh is very fine and the mesh 1000 shows also low values, but then again it is dependent on the bathymetry for its computation.

Because of this, we place two new points instead of Cardwell and Clump Point, both located 1.5 km away from the coast at the original point. This way we minimize the bathymetry's impact on the local results while still keeping the results close to what is measured.

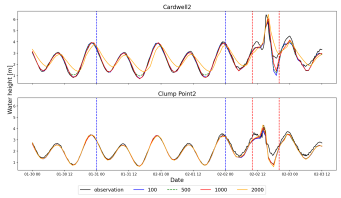

(a) Simulation results entire time series, using meshes 100, 500, 1000 and 2000 in blue, green, red and yellow respectively. Regular RMSE period is between blue dotted lines and landfall period is between the red.

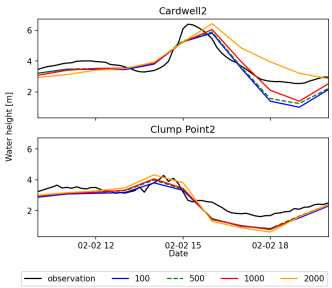

(b) Close-up of Figure 3.13a during cyclone period (red dotted lines).

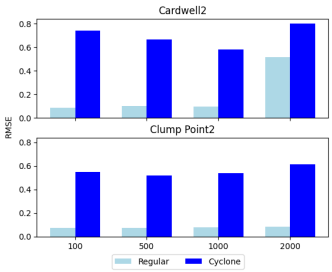

(c) RMSE between observation and simulations, RMSE for regular period in light blue and in darker blue for the landfall period.

Figure 3.13: Results for the new validation points, entire time series (left) and close-up of landfall period (center) and RMSE for each of the simulations and observation, for both time periods described in 3.13a (right).

3.3.2 Inundated areas and mesh resolution

Looking at inundation maps, the results in term of area are quite different. In Figure 3.14, we see a clear deterioration in the quality of the simulation. The area becomes very large when the mesh coarsens. Looking at the topographic maps after smoothing of the same region for the same meshes, we see that the coast is close to flat for the coarsest mesh (mesh 2000) (Figure 3.15, right). We also see that the coast gets swallowed by what we display as sea in the figures, which is in reality the elements where the bathymetry is positive (topography < 0). The smoothing and the mesh sizes are the only thing that changes between the topographic maps. The smoothing is applied to avoid numerical errors, a coarser mesh needs a stronger smoothing (without smoothing the simulations cannot run).

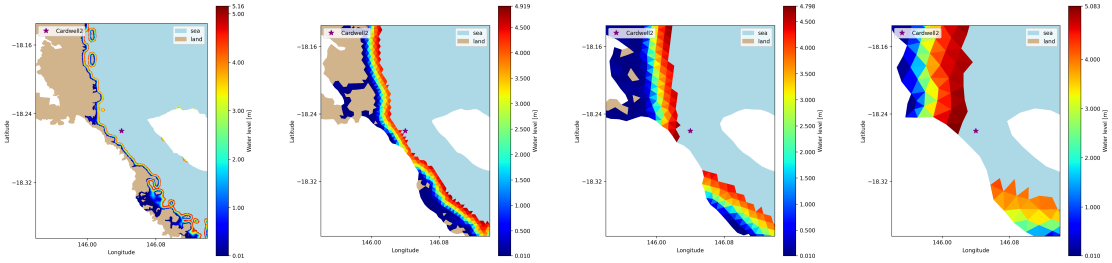

(a) Mesh 100 (b) Mesh 500 (c) Mesh 1000 (d) Mesh 2000

Figure 3.14: Inundations maps of the region around Cardwell. Simulation results using meshes with increasing element size from left to right, mesh 100 (left), mesh 500 (center left), mesh 1000 (center right) and mesh 2000 (right). Each graph has its own colorbar as the maximums are not equal

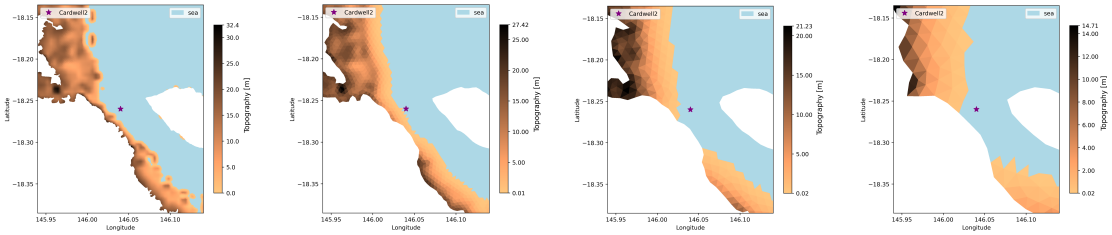

(a) Mesh 100 (b) Mesh 500 (c) Mesh 1000 (d) Mesh 2000

Figure 3.15: Topography of the region around Cardwell after smoothing, land is in shades of brown and sea is in blue. The second validation point (Cardwell 2) is shown as the purple star.

We also include figures of the entire domain. In the previous section, these were difficult to visualize due to the domain's size relative to the flooded areas. However, they are now clearer with the use of coarser meshes. As we could already see in Figure 3.14, we observe in Figure 3.16 the submerged area growing substantially with the mesh coarsening.

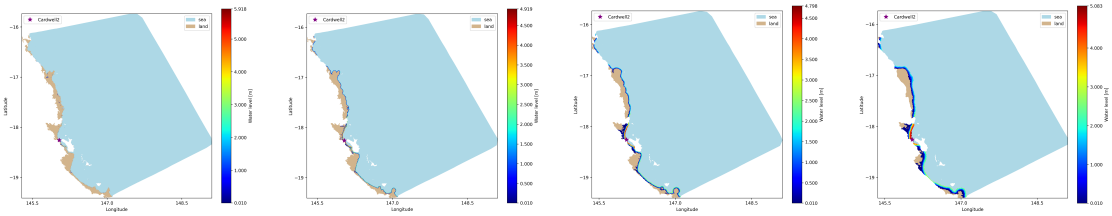

(a) Mesh 100 (b) Mesh 500 (c) Mesh 1000 (d) Mesh 2000

Figure 3.16: Simulation results on the entire domain, sea and land are in blue and tan respectively. The second validation point (Cardwell 2) is shown as the purple star.

To summarize the results in this section regarding the relation between mesh resolution and result quality, we show Figure 3.17 representing the behavior of the simulation results when increasing the mesh size. For Cardwell (left) the submerged area grows rapidly with the mesh size, up until it reaches a threshold, where inundatable areas are flooded. In addition to this, the smoothing of the bathymetry causes the land to disappear giving way to the sea. This also shows for the impacted population as it rises significantly with the first coarsening of the mesh, then reduces as the city becomes under water partially then totally, resulting in the population no longer being counted. On a global note, for the entire domain, the submerged area (blue) increase steadily as the mesh is less refined. The population follows and seems to rise less steeply in the end, as for the local case of Cardwell. Table 3.2 groups runtime information for each simulation, showing a runtime ranging from 8 hours for mesh 100 to a few minutes for the

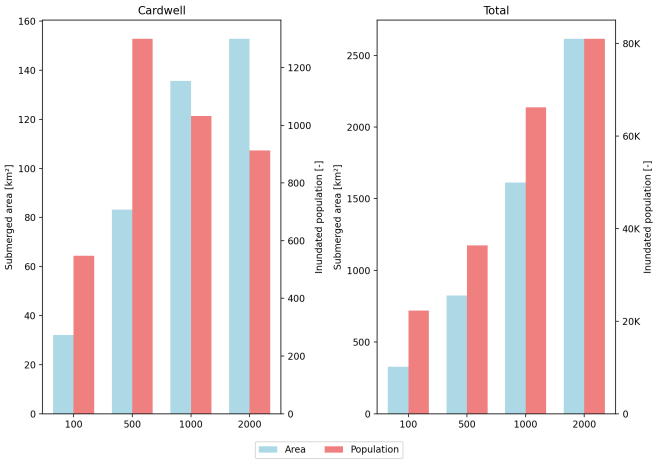

Figure 3.17: Submerged area (blue) and population impacted by the cyclone (red) for the different mesh sizes, in Cardwell (left) and on the entire domain (right).

coarsest mesh. It also shows that the runtimes for the mesh 500 and the mesh 1000 simulations to be quite close.

Computation Information	**Mesh 100**	**Mesh 500**	**Mesh 1000**	**Mesh 2000**
Number of triangles	$3\,M$	$120\,k$	$100\,k$	$28\,k$
Computation time	$8\,[H]$	$4\,[min]$	$5\,[min]$	$2\,[min]$

Table 3.2: Computation information for each mesh.

3.4 Track refinement's impact on results

In this section we present the results from a simulation with a mesh that is not refined along the track, mesh 100 without track in section 2.1.3. First we show the validation observations and simulation results at these sites. Then we briefly show inundation maps for this simulation.

In Figure 3.18, the results of the simulation with the mesh that is not refined along the track (no track simulation) have the same shape as the observations outside the time period where Yasi hits land. Inside that time period (between red dotted lines) however, the results are rather far from the observations and the simulation with track, for the sites where a real surge is measured (Cardwell and Clump Point). In the sites where the measured surge is less consequent, the no track simulation performs as well as the simulation with track refinement. This also shows in the RMSE histograms in Figure 3.19b, they are almost the same for

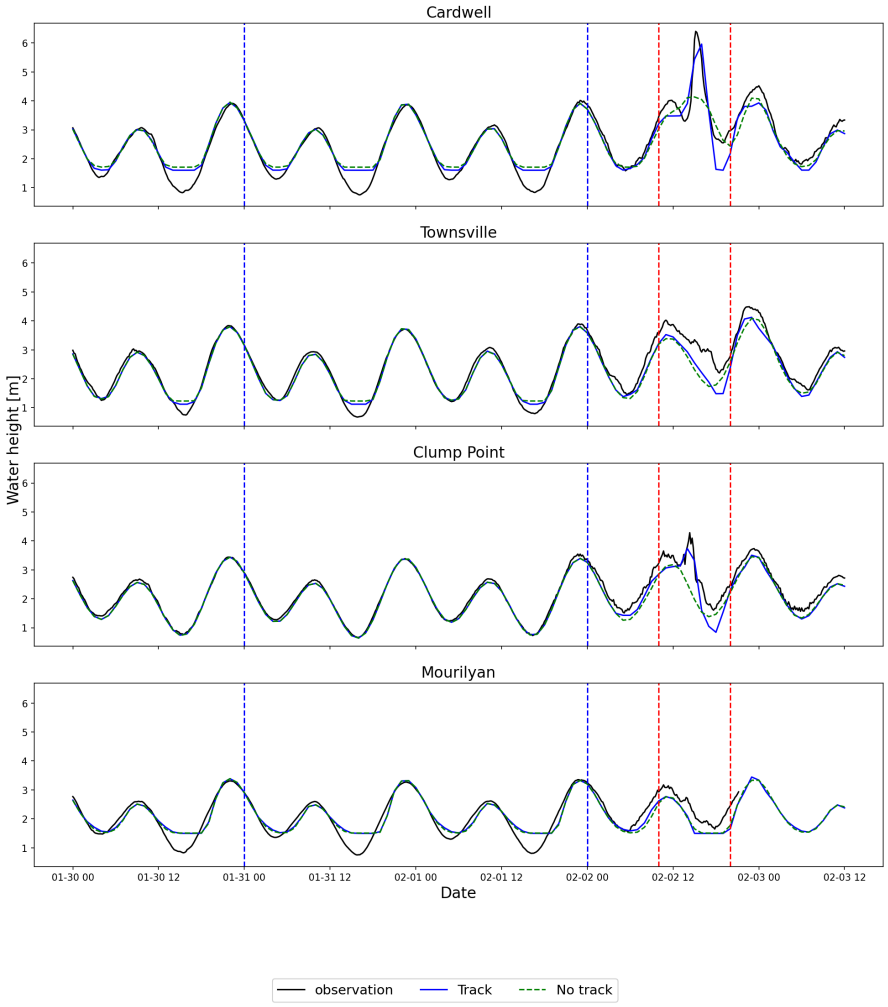

Figure 3.18: Time series of water height from observations (black), and for simulations using mesh 100 (blue) and mesh no track (green). Regular RMSE period is between blue dotted lines and landfall is between the red.

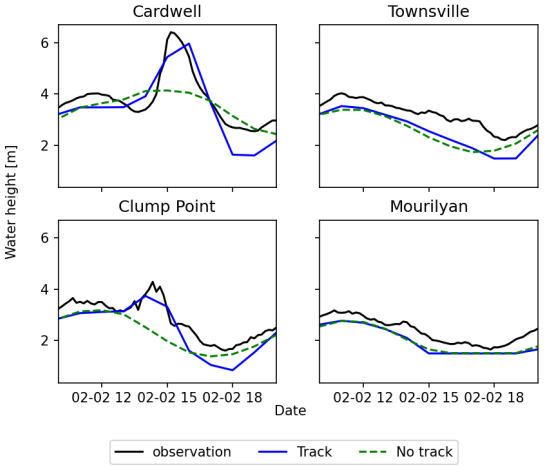

(a) Close-up of Figure 3.18 during cyclone period (red dotted lines), results of the simulations using meshes with minimal size 100, with (blue) and without (green) refinement along cyclone track.

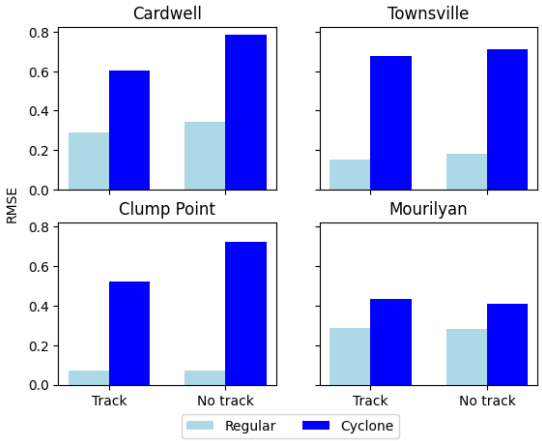

(b) RMSE between observation and simulations, RMSE for regular period (in blue in Figure 3.18) in light blue and in darker blue for the landfall period.

Figure 3.19: Close-up of Figure 3.19a (left) and RMSE for each of the simulations with relation to observations, for both time periods described in Figure 3.18 (right).

both simulations in the right column. In the left column, the Cyclone RMSE for the simulation without refinement along the track is higher than that for the track simulation by 30 %.

We look at close-ups of the inundations around the regions of Cardwell and Townsville in Figure 3.20 and Figure 3.21.

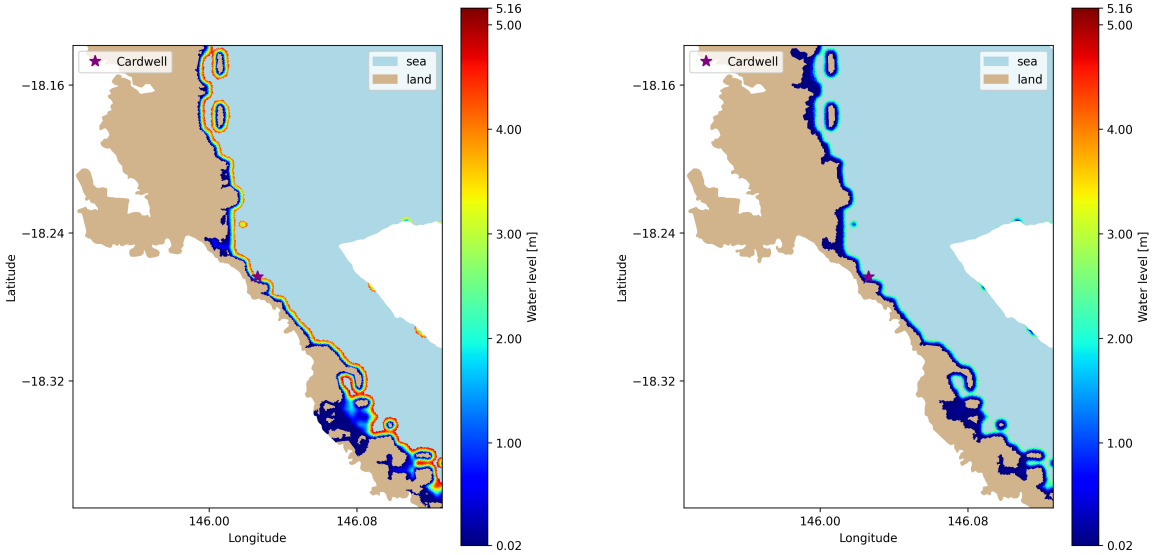

(a) Inundation map for simulation using the mesh with refinement along track.

(b) Inundation map for simulation using mesh without refinement along track.

Figure 3.20: Close-up on inundation maps in Cardwell, simulation with mesh with (left) and without (right) refinement along track.

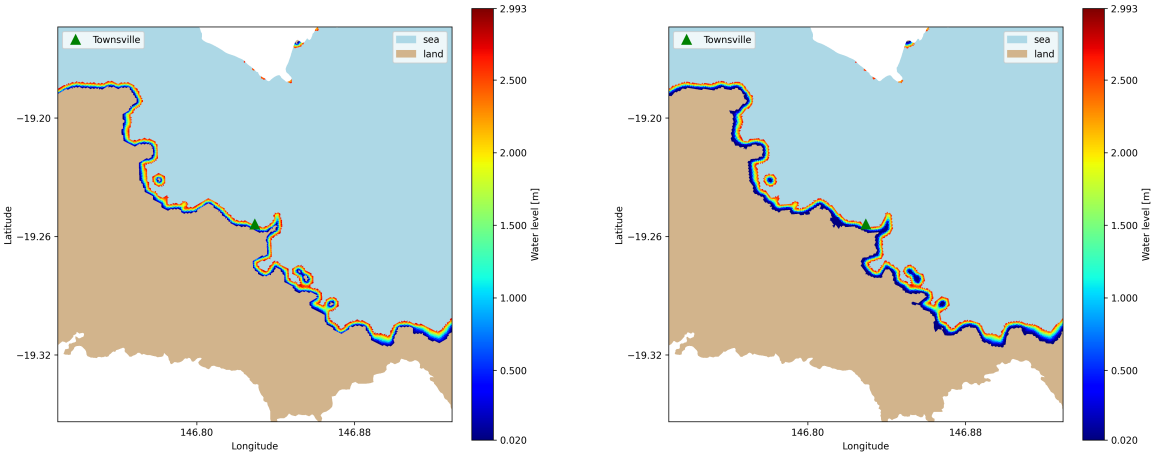

(a) Inundation map for simulation using the mesh with refinement along track.

(b) Inundation map for simulation using the mesh without refinement along track.

Figure 3.21: Close-up on inundation maps in Townsville, simulation with mesh with (left) and without (right) refinement along track.

Although the inundation maps are similar there are significant differences. We clearly observe Cardwell to be less flooded according to the simulation without mesh refinement along track in Figure 3.20b, we also observe that overall the water level is lower for that simulation compared to the simulation using the mesh refined along the track.

In Figure 3.21 however, we observe slightly more flooding with the mesh without refinement along track than for the mesh with refinement.

We summarize the submerged areas for these regions and the entire domain, for these two setups in Figure 3.22. The total area submerged by the storm surge is larger for the simulation using the mesh without track refinement.

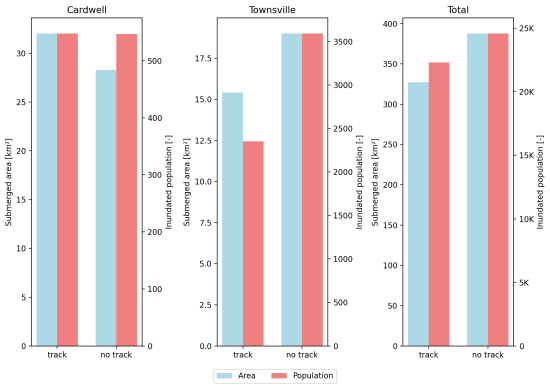

Figure 3.22: Submerged area and population impacted by the surge, close-up on Cardwell (left), on Townsville (center) and entire domain (right) for simulations with mesh with and without track refinement.

3.5 Cyclone and tide interaction

In this section we keep the base model setup from the previous section, the most refined mesh (mesh 100) and wind forcings using a Holland's model with track data from JTWC. We now compare the hypothetical case where Yasi makes landfall at a different time, to observe the interaction between the tide and the storm surge. We first go through the validation points again as for the previous sections, and then we cover the inundation maps, zooming in on Cardwell, and looking at flooding numbers.

Figure 3.23 shows the simulations results at the validation points, Cardwell (top left), Townsville (top right), Clump Point (bottom left) and Mourilyan (bottom

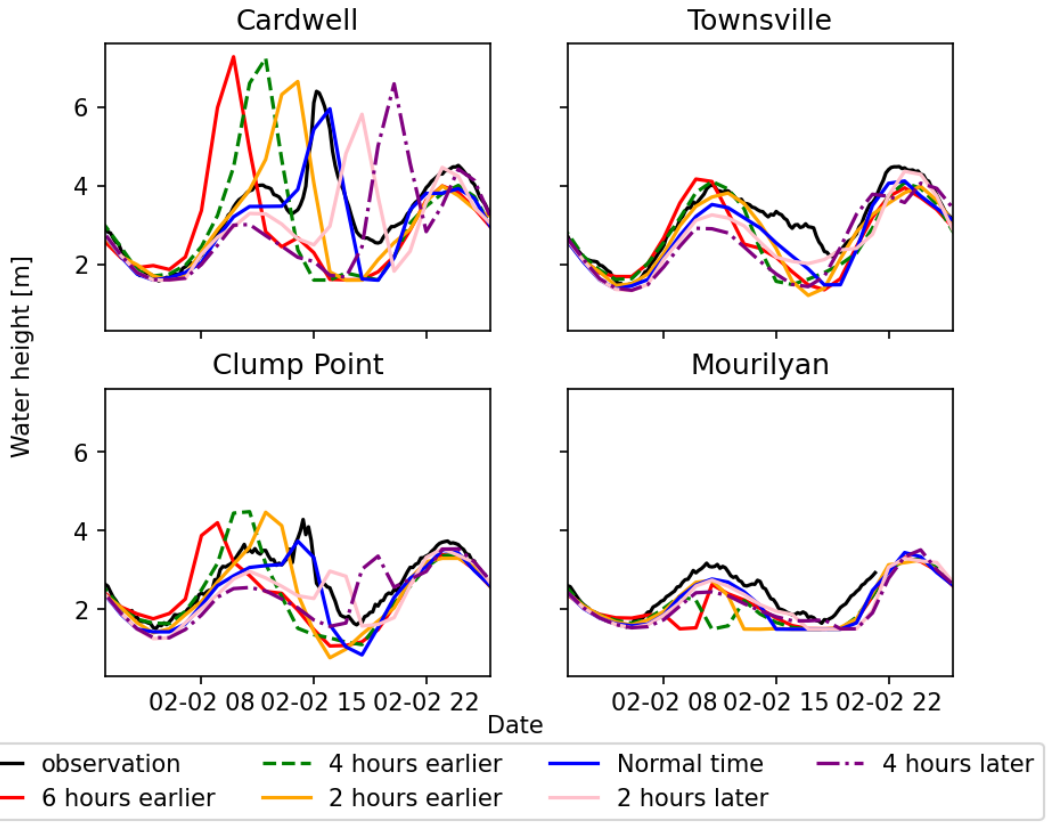

Figure 3.23: Close-up on simulated and observed water heights during the surge at validation points: Cardwell (top left), Townsville (top right), Clump Point (bottom left), and Mourilyan (bottom right). The figure compares observed water levels (black) with simulated results for cyclone landfall timings: 6 hours earlier (red), 4 hours earlier (green), 2 hours earlier (yellow), normal time (blue), 2 hours later (pink), and 4 hours later (purple).

right). Each line represents a simulation with a specific cyclone landfall time. The first simulation models a cyclone making landfall 6 hours earlier than the observed event. The simulations are staggered at 2 hours intervals, with the final simulation representing a cyclone with landfall delayed by 4 hours. This way we have simulations with landfall in a 12 hours span, covering an entire tidal cycle.

Figure 3.23 focuses specifically on the storm surge period. This close-up view highlights the differences in surge magnitude under varying cyclone landfall scenarios. We can already observe that the simulations that have cyclone landfall during the high tide have a higher peak (for Cardwell and Clump Point) than what is measured. These are the simulations with an advanced cyclone of 6 hours (red), 4 hours (green) and 2 hours (yellow). The lines that show the smaller peak surge are the "Normal time" (blue) and the 2 hours later (pink), these are the simulations for

which the cyclone arrives during low tide or during the lowering of the tide. The periods where the tide is growing all show a stronger surge than the mere sum of the basic surge and the tide raise. For the red line, the storm surge is 1 m higher than the observed surge, the tide is at the same level when the cyclone hits, the only difference being that the tide is rising instead of falling.

We do not show the RMSE between the observations and the simulations as these are hypothetical scenarios that did not take place, the observation are mainly there as visual guidance.

We look at inundation maps of Cardwell in Figure 3.24. We observe the flooding to be larger in the cases where the cyclone hits during the rise of the tide in Figure 3.24a and Figure 3.24f. These are the simulations where we observe the largest submerged area. However the peak surge is observed for the simulation in Figure 3.24b, taking place at a high tide.

In figure 3.25, we present the submerged areas (blue) and the impacted population (red) for the different cyclone timing scenarios, for Cardwell (left) and the total domain (right). This shows the impact of tidal cycle on the surge. The submerged areas are up to 50% larger when the tide is rising, in this simulation it happens 6 hours before and 4 hours after the actual landfall of Yasi.

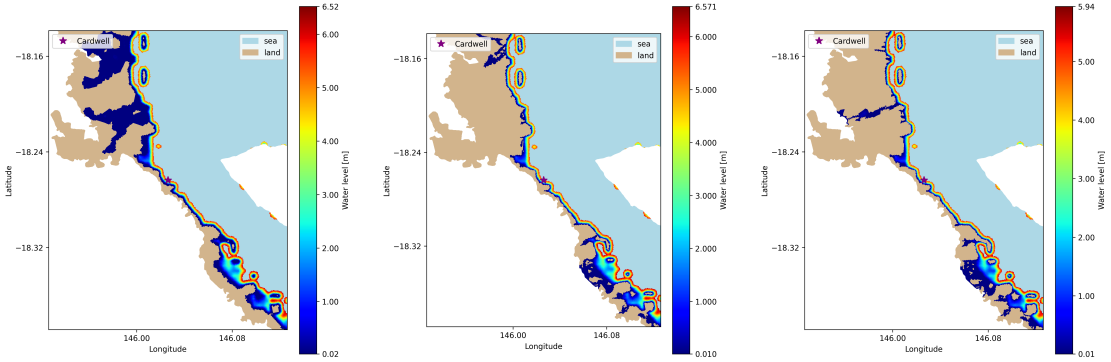

(a) Hypothetical case where Yasi hits 6 hours earlier.

(b) Hypothetical case where Yasi hits 4 hours earlier.

(c) Hypothetical case where Yasi hits 2 hours earlier.

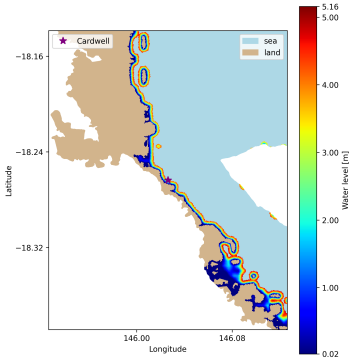

(d) True timing of the Yasi landfall.

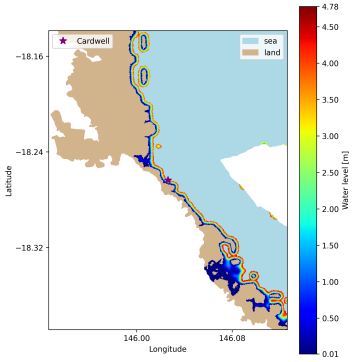

(e) Hypothetical case where Yasi hits 2 hours later.

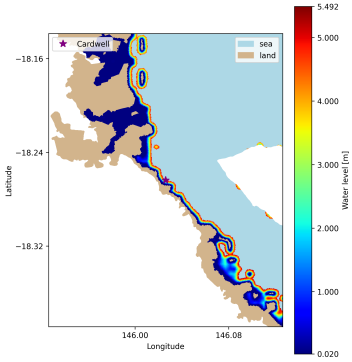

(f) Hypothetical case where Yasi hits 4 hours later.

Figure 3.24: Inundation maps centered on Cardwell (purple star) for each of the cyclone timing scenarios. Note: The colorbars are different to show the peak surge.

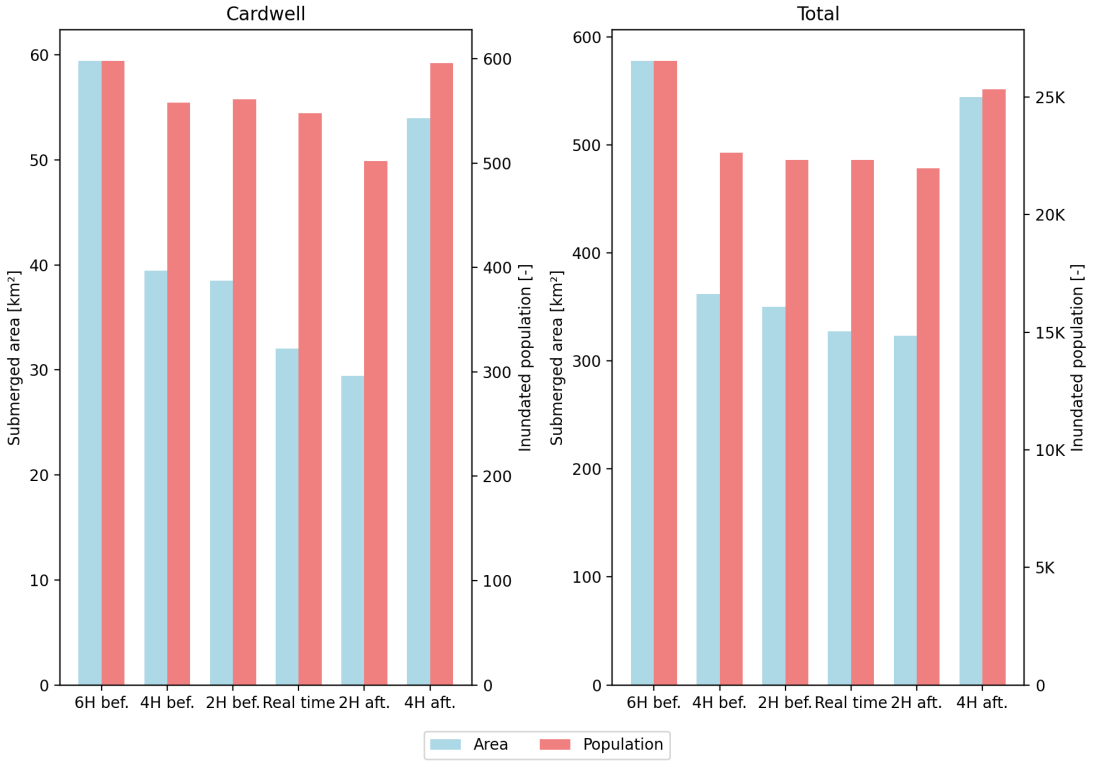

Figure 3.25: Submerged areas and impacted population, for the close-up on Cardwell (left) and the entire domain (right). Simulations with landfall occurring in a range from 6 hours before to 4 hours after the observed event.

Chapter 4

Discussion

In this chapter, we discuss the results presented in the previous chapter. We examine how the results address the objectives of our project outlined in chapter 1.

4.1 Hydrodynamic model for surge modeling

During the process we found that it is not enough to only use the base data models, Era5 and eReefs, for wind and pressure profiles. For extreme conditions, it is necessary to use a cyclone model, such as Holland's model. We showed in section 2.2.1 that this model is quite close to the observations, as we expected (Lin and Chavas, 2012). We saw that when using the track data from the Joint Typhoon Warning Center (JTWC) we overshot the wind speed, however we believe this shouldn't impact the result negatively due to the wind drag saturation at high wind speed (Powell et al., 2003).

Unfortunately it is difficult to have clear validation data for the areas that are flooded by the storm surge. Satellite pictures are often blocked by the heavy clouds the cyclone transports. This leaves us little to work with in terms of validation of the submerged areas. However, we can work with the numerous storm surge monitoring sites deployed by Queensland's government. These give us a good idea of what the surge should look like at certain key locations.

We find, with our SLIM model, the results at the locations of the validation sites to be convincing. The surge is clearly visible at the moment the cyclone hits land (Figure 3.2). The RMSEs presented in this chapter also confirms that track data from JTWC is the better option. Possibly for other cyclones the track data from the Australian Bureau of Meteorology (BOM) could provide better results, but in this case, for cyclones Yasi and Ita (for wind and pressure validation), JTWC

performs best. We are satisfied to see that the results are so close to observations, the water level only being off by 30 cm when the storm surge is at its peak. The SLOSH model surge height is known to be within 20% of observed peak surge (Jelesnianski et al., 1992). Here, with a storm surge of about 3 m above the tide, we are within 10% of what is measured, and this is for Cardwell, where the storm surge was highest. For the other monitoring sites the results are even more satisfying. The RMSEs are good indicators, however we should also watch the time series as the model describes a surge that retracts slightly faster than what is observed.

In this context, we believe this a good step towards considering the model to be valid. However, it should be analyzed further for other cyclones.

4.2 Mesh refinement

In the section 3.3 we showed how the quality of the results deprecates with the mesh size and refinement. We observed that the key elements here are the representation of the bathymetry and the topography. The bathymetry provided by Deepreef has a very good resolution, but it is considerably modified by the smoothing operation and also by the overall fact that with larger elements we might ignore some physical aspects as small hills or dunes. Thus the model would not interact with these elements. The model overall showed rather good results in the comparisons with observations from storm surge monitoring sites even for coarse meshes. However the areas shown to be flooded were not realistic nor in line with what we found with the most refined mesh which we believe is closest to reality. This poses a new question about the validation process: is it sufficient to rely solely on measurement sites located along the coastline to assess the accuracy of a storm surge model?

Looking at the results from section 3.4 we also observe the fact that the simulated inundation is larger when the mesh is not refined along the track. It shows that the cyclone's wind and pressure forcings are somewhat smoothed and that they spread the flooding over a larger part of the coastline, whereas the main flooding would take place near the landfall region for a track refined mesh. This is important to take into account, especially in the case we want to build a risk map over the entirety of the coast following probabilistic or an ensemble approach. To achieve such a map, it is needed to simulate many cyclones. In these processes, the results would be more accurate if the simulations used a mesh refined along the track of each cyclone. Otherwise the risk map would undershoot the danger or the simulations would need to have a very refined mesh everywhere, which wouldn't be computationally ideal. The simulations using the mesh with elements of size

1000 and 2000 showed it could be sufficient to limit the size of the elements along the track to 1000 or 2000 m, at least to observe the storm surge. This would save computation time.

4.3 Tide interaction with storm surge

As we show in section 3.5, the surge would have been higher had the cyclone hit at another time. The flooded area are strongly influenced by the tides, not only by the water height itself, but especially by the motion the tide brings to the surge. Results show that the flooded area could grow by up to 50% if the cyclone hits during the rise of the tide. The largest surges in our simulations appear around 3 to 5 hours prior to the high tide. In an ensemble or probabilistic approach, the process of building risk maps, which are of high interest for authorities, risk managers, engineers and insurers, needs to take account of the time the cyclone makes its landfall. This is also the conclusion brought by Horsburgh and Wilson, 2007.

4.4 Limitations and future perspectives

This model shows good results, however, the absence of validation data for the inundated areas limits the possibility of confirmation for model. If we could use more detailed validation data such as clear satellite imagery, possibly radar measurements of inundated areas, or water level measurements from monitoring sites further inland, we could perhaps have more confidence in the simulation results.

In this work, we estimated the number of people that would be impacted by the storm surge according to the simulations. However the method we use for the estimation has certain limitations, due to the nature of our population data, which is presented in discrete hexagons. For our estimation a population center (hexagon) is considered flooded only if its center is submerged. There may be cases where a zone is classified as flooded even if only the very center is submerged, while the opposite scenario can also occur, where a largely flooded population center is excluded when its center is dry. In coastal cities such as Cardwell, the hexagons that are closest to the sea are almost automatically taken into account as flooded. Which is why we have a high number of impacted inhabitants even for the Era5 and eReefs winds and pressures, that show low submerged areas. Other indicators of the damage the surge brings could be interesting, such as the mapping of electrical lines, fragile bridges or roads in general, and of course harbors, that suffer terribly

from storm surges.

The SLIM 2D model also has its limitations, as it ignores the 3D flows, and it doesn't replace the waves. But using SLIM 3D with a wetting and drying setup isn't possible yet. A solution to that could be to link SLIM2D with SWAN model from Delft University as made in Dobbelaere et al., 2022.

Our model does not take account of the heavy rainfall that comes the cyclone, which adds to the storm surge thus causing larger flooding.

Since the bathymetry and its smoothing have a large impact on the quality of the results, it would be interesting to see the results of simulations without a smoothing. While not possible yet, trying to stabilize the model for simulations without (or with reduced) smoothing of the bathymetry could be a possible improvement for the future.

In addition to that, we observed that an update of `seamsh`, which we use for mesh generation, caused some simulations to be instable. To avoid this instability the simulations were computed using longs instead of floats, multiplying the runtime on GPUs by 4.

This being said, the work sets a first step in the long process of model validation for large-scale usage, such as in an ensemble approach with the objective of creating risk maps for the Great Barrier Reef.

Chapter 5

Conclusion

In this study, we first defined the importance of storm surge modeling. The cyclone intensification and the sea level rise, due to the climate change, constitute a real threat for low-lying coastal areas. Using storm surge models to build risk maps, showing the areas possibly at risk of inundation, allows for better decision-making by the authorities and insurance companies.

We crafted a model by first defining a simulation domain for the case of cyclone Yasi on a selected part of the Great Barrier Reef. Then we built meshes of different refinements using `seamsh`. Using these meshes and different wind forcing parameters we ran several simulations with the 2D SLIM Hydrodynamic model, in order to obtain results in the form of water height time series at selected measurement sites. We also created inundation maps and estimated the size of submerged areas. The simulated time series were satisfying. As we had no observed inundation area measurements, the inundation maps mainly served as visualizing tools, and in some cases facilitated comparisons between simulations.

During this process we came across a few parameters that play a key role in the simulation of storm surges. First we highlighted the necessity to use a cyclone model to represent the wind and pressure profile, in our model, the Holland's model with cyclone track from JTWC proved to work well.

Additionally, we observed that the mesh resolution has an indirect impact on the simulation result, through the impact it has on bathymetry quality. The bathymetry loses some details as it is projected on the mesh. The smoothing then applied on this projected bathymetry, allowing a stable simulation, reduces the quality of the bathymetry further. This was very visible on the inundation maps, and less noticeable in the time series at measuring sites.

Furthermore, we showed the importance to have a consistent and relatively small size of mesh elements on the cyclone track to allow for better results. The element size of the mesh should be capped at 1000 m around the cyclone track, it was the maximum element size along track for which the simulations showed results in line with observation.

We also highlighted how the storm surge interacts with the tide cycle: for a selected cyclone track, the peak storm surge is observed if the landfall occurs 3 to 5 hours prior to the high tide, during the rise of the tide.

The results of this study are not sufficient on their own for creating probability maps for risk analysis, however they could serve for further investigation and studies of storm surges simulation using SLIM.

Bibliography

Arcement, J., George J., & Schneider, V. R. (1990). *Guide for selecting manning's roughness coefficients for natural channels and flood plains* (Water-Supply Paper No. 2339) (Accessed: 2025-01-03). United States Geological Survey (USGS). Washington, D.C., USGS. https://pubs.usgs.gov/wsp/2339/report.pdf

Arthur, W. C. (2021). A statistical–parametric model of tropical cyclones for hazard assessment. *Natural Hazards and Earth System Sciences*, *21*(3), 893–916. https://doi.org/10.5194/nhess-21-893-2021

Australian Bureau of Meteorology (BoM). (2023). Tropical cyclone track and data — BoM services [Accessed on 26-12-2024].

Australian Institute for Disaster Resilience. (2011). Cyclone yasi, queensland, 2011 [Accessed: 2025-01-05]. https://knowledge.aidr.org.au/resources/cyclone-cyclone-yasi-queensland-2011/

Australian Institute for Disaster Resilience. (2015). Cyclone marcia, queensland, 2015 [Accessed: 2025-01-05]. https://knowledge.aidr.org.au/resources/cyclone-cyclone-marcia-queensland/

Australian Institute of Marine Science (AIMS). (2020). Northern australia automated marine weather and oceanographic stations, sites: [lizard island], parameters: [air pressure, wind speed] [Accessed: 2025-01-03]. https://doi.org/10.25845/5c09bf93f315d

Beaman, R. J. (2010). *Project 3d-gbr: A high-resolution depth model for the great barrier reef and coral sea* (tech. rep. No. Project 2.5i.1a Final Report) (pp. 13 plus Appendix 1.). Marine and Tropical Sciences Research Facility (MTSRF). Cairns, Australia. https://www.deepreef.org/2010/08/13/3dgbr-final/

Chamberlain, M. A., Oke, P. R., Fiedler, R. A. S., Beggs, H. M., Brassington, G. B., & Divakaran, P. (2021). Next generation of bluelink ocean reanalysis with multiscale data assimilation: Bran2020. *Earth System Science Data*, *13*(12), 5663–5688. https://doi.org/10.5194/essd-13-5663-2021

CIRCulation, A. ((ADCIRC)). Adcirc: Advanced circulation model. https://adcirc.org/

Commonwealth of Australia (Geoscience Australia). (2021). Population density map, geoscience australia [© Commonwealth of Australia (Geoscience Australia) 2021].

Courant, R., Friedrichs, K., & Lewy, H. (1967). On the partial difference equations of mathematical physics. *IBM Journal of Research and Development*, *11*(2), 215–234. https://doi.org/10.1147/rd.112.0215

Delandmeter, P., Lambrechts, J., Marmorino, G. O., Legat, V., Wolanski, E., Remacle, J.-F., Chen, W., & Deleersnijder, E. (2017). Submesoscale tidal eddies in the wake of coral islands and reefs: Satellite data and numerical modelling. *Ocean Dynamics*, *67*(7), 897–913. https://doi.org/10.1007/s10236-017-1066-z

Dobbelaere, T., Curcic, M., Le Hénaff, M., & Hanert, E. (2022). Impacts of hurricane irma (2017) on wave-induced ocean transport processes. *Ocean Modelling*, *171*, 101947. https://doi.org/10.1016/j.ocemod.2022.101947

Egbert, G. D., & Erofeeva, S. Y. (2002). Efficient inverse modeling of barotropic ocean tides. *Journal of Atmospheric and Oceanic Technology*, *19*(2), 183–204. https://doi.org/10.1175/1520-0426(2002)019<0183:EIMOBO>2.0.CO;2

Faryuni, I. D., Saint-Amand, A., Dobbelaere, T., Umar, W., Jompa, J., Moore, A. M., & Hanert, E. (2024). Assessing coral reef conservation planning in wakatobi national park (indonesia) from larval connectivity networks. *Coral Reefs*, *43*(1), 19–33. https://doi.org/10.1007/s00338-023-02443-y

Figueiredo, J., Thomas, C. J., Deleersnijder, E., Lambrechts, J., Baird, A. H., Connolly, S. R., & Hanert, E. (2022). Global warming decreases connectivity among coral populations. *Nature Climate Change*, *12*(1), 83–87. https://doi.org/10.1038/s41558-021-01248-7

GEBCO Bathymetric Compilation Group. (2024, July 4). *The gebco_2024 grid – a continuous terrain model of the global oceans and land* [Language: en. Accessed: 2024-07-04 14:12]. NERC EDS British Oceanographic Data Centre NOC. https://doi.org/10.5285/1c44ce99-0a0d-5f4f-e063-7086abc0ea0f

Geuzaine, C., & Remacle, J.-F. (2009). Gmsh: A 3-d finite element mesh generator with built-in pre- and post-processing facilities. *International Journal for Numerical Methods in Engineering*, *79*, 1309–1331. https://doi.org/10.1002/nme.2579

Gourgue, O., Baeyens, W., Chen, M., de Brauwere, A., de Brye, B., Deleersnijder, E., Elskens, M., & Legat, V. (2013). A depth-averaged two-dimensional sediment transport model for environmental studies in the scheldt estuary and tidal river network. *Journal of Marine Systems*, *128*, 27–39. https://doi.org/https://doi.org/10.1016/j.jmarsys.2013.03.014

Gourgue, O., Comblen, R., Lambrechts, J., Kärnä, T., Legat, V., & Deleersnijder, E. (2009). A flux-limiting wetting–drying method for finite-element shallow-

water models, with application to the scheldt estuary. *Advances in Water Resources*, *32*(12), 1726–1739. https://doi.org/10.1016/j.advwatres.2009.09.005

Government, Q. (2012). *Tropical cyclone yasi - 2011 post cyclone coastal field investigation* (tech. rep.). Department of Science, Information Technology, Innovation and the Arts. Brisbane, Australia. http://www.longpaddock.qld.gov.au/about/publications/index.html

Gray, W. M. (1998). The formation of tropical cyclones. *Meteorology and Atmospheric Physics*, *67*(1), 37–69. https://doi.org/10.1007/BF01277501

Hersbach, H., Bell, B., Berrisford, P., Biavati, G., Horányi, A., Muñoz Sabater, J., Nicolas, J., Peubey, C., Radu, R., Rozum, I., Schepers, D., Simmons, A., Soci, C., Dee, D., & Thépaut, J.-N. (2023). *Era5 hourly data on single levels from 1940 to present* [Accessed on 25-12-2024]. Copernicus Climate Change Service (C3S) Climate Data Store (CDS). https://doi.org/10.24381/cds.adbb2d47

Holland, G. J. (1980). An analytic model of the wind and pressure profiles in hurricanes. *Monthly Weather Review*, *108*, 1212–1218. https://doi.org/10.1175/1520-0493(1980)108<1212:AAMOTW>2.0.CO;2

Horsburgh, K. J., & Wilson, C. (2007). Tide-surge interaction and its role in the distribution of surge residuals in the north sea. *Journal of Geophysical Research: Oceans*, *112*(C8). https://doi.org/https://doi.org/10.1029/2006JC004033

IPCC. (2021). *Climate change 2021: The physical science basis* [Contribution of Working Group I to the Sixth Assessment Report of the Intergovernmental Panel on Climate Change]. Cambridge University Press. https://www.ipcc.ch/report/ar6/wg1/

Jelesnianski, C. P., Chen, J., & Shaffer, W. A. (1992). *Slosh: Sea, lake, and overland surges from hurricanes* (tech. rep. No. 48). United States, National Weather Service. https://repository.library.noaa.gov/view/noaa/7235

Joint Typhoon Warning Center (JTWC). (2023). Tropical cyclone best-track data [Accessed on 26-12-2024]. https://www.metoc.navy.mil/jtwc/jtwc.html

Knabb, R. D., Rhome, J. R., & Brown, D. P. (2023). *Tropical cyclone report: Hurricane katrina (23–30 august 2005)* (tech. rep.). National Hurricane Center. https://www.nhc.noaa.gov/data/tcr/AL122005_Katrina.pdf

Kontur. (2023). Population density in australia using 400m h3 hexagons. https://data.humdata.org/dataset/kontur-population-australia

Lambrechts, J., Hanert, E., Deleersnijder, E., Bernard, P.-E., Legat, V., Remacle, J.-F., & Wolanski, E. (2008). A multi-scale model of the hydrodynamics of the whole great barrier reef. *Estuarine, Coastal and Shelf Science*, *79*(1), 143–151. https://doi.org/10.1016/j.ecss.2008.03.016

Legrand, S., Deleersnijder, E., Delhez, E., & Legat, V. (2007). Unstructured, anisotropic mesh generation for the northwestern european continental shelf, the continental slope and the neighbouring ocean [Recent Developments in Physical Oceanographic Modelling: Part IV]. *Continental Shelf Research*, *27*(9), 1344–1356. https://doi.org/https://doi.org/10.1016/j.csr.2007.01.009

Legrand, S., Deleersnijder, E., Hanert, E., & Wolanski, E. (2006). High-resolution, unstructured meshes for hydrodynamic models of the great barrier reef, australia. *Estuarine Coastal and Shelf Science*, *68*, 36–46. https://doi.org/10.1016/j.ecss.2005.08.017

Lin, N., & Chavas, D. (2012). On hurricane parametric wind and applications in storm surge modeling. *Journal of Geophysical Research: Atmospheres*, *117*(D9). https://doi.org/10.1029/2011JD017126

Liu, B., Guan, C., & Xie, L. (2012). The wave state and sea spray related parameterization of wind stress applicable from low to extreme winds. *Journal of Geophysical Research (Oceans)*, *117*. https://doi.org/10.1029/2011JC007786

Moon, I.-J., Ginis, I., & Hara, T. (2004). Effect of surface waves on air–sea momentum exchange. part ii: Behavior of drag coefficient under tropical cyclones. *Journal of the Atmospheric Sciences*, *61*(19), 2334–2348. https://doi.org/10.1175/1520-0469(2004)061<2334:EOSWOA>2.0.CO;2

Moon, I.-J., Ginis, I., Hara, T., & Thomas, B. (2007). A physics-based parameterization of air-sea momentum flux at high wind speeds and its impact on hurricane intensity predictions. *Monthly Weather Review*, *135*(8), 2869–2878. https://doi.org/10.1175/MWR3432.1

Munksgaard, N. C., Zwart, C., Kurita, N., Bass, A., Nott, J., & Bird, M. I. (2015). Stable isotope anatomy of tropical cyclone ita, north-eastern australia, april 2014. *PLOS ONE*, *10*(3), 1–15. https://doi.org/10.1371/journal.pone.0119728

NASA. (2000). Shuttle radar topography mission (srtm) version 2. http://www2.jpl.nasa.gov/srtm/

National Hurricane Center. (NHC). About the saffir-simpson hurricane wind scale [Accessed: 2025-01-04]. https://www.nhc.noaa.gov/aboutsshws.php?ftag=MSF0951a18

National Oceanic and Atmospheric Administration. ((NOAA)). Storm surge modeling and mapping. https://vlab.noaa.gov/web/mdl/storm-surge

Nott, J. (2011). A 6000 year tropical cyclone record from western australia. *Quaternary Science Reviews*, *30*(5), 713–722. https://doi.org/10.1016/j.quascirev.2010.12.004

OpenStreetMap Contributors. (2024). OpenStreetMap (Screenshot) [Map data ©OpenStreetMap contributors, under the Open Database License (ODbL). Accessed on (25/12/24).].

OpenTopography. (2024). Srtm 30m dem data access [Accessed on [03/01/2025]]. https://opentopography.org/

Ortleb, S., Lambrechts, J., & Kärnä, T. (2022). Wetting and dryingwetting and drying procedures for shallow water simulations. In H. Schuttelaars, A. Heemink, & E. Deleersnijder (Eds.), *The mathematics of marine modelling: Water, solute and particle dynamics in estuaries and shallow seas* (pp. 287–314). Springer International Publishing. https://doi.org/10.1007/978-3-031-09559-7_11

Pietrzak, J., Deleersnijder, E., & Schröter, J. (2005). Preface: Special issue: The second international workshop on unstructured mesh numerical modelling of coastal, shelf and ocean flows. *Ocean Modelling*, *10*, 1–3.

Powell, M., Vickery, P., & Reinhold, T. (2003). Reduced drag coefficient for high wind speeds in tropical cyclones. *Nature*, *422*, 279–83. https://doi.org/10.1038/nature01481

QGIS Development Team. (2024). *Qgis geographic information system*. QGIS Association. https://www.qgis.org

Queensland Government. (2011). Storm surge information for queensland [Monitoring devices installed in 2011. Accessed: 29-12-2024]. https://www.qld.gov.au/environment/coasts-waterways/beach/storm/storm-explained

Queensland Government. (2015). Cairns tide gauge archived interval recordings [Data recorded in 2011. Accessed: 29-12-2024]. https://www.data.qld.gov.au/dataset/cairns-tide-gauge-archived-interval-recordings

Randresihaja, N. R., Gourgue, O., Alaerts, L., Lambrechts, J., Court, M. D. L., Fettweis, X., Grégoire, M., & Hanert, E. (2025). *Assessing the sensitivity of storm surge simulation to the atmospheric forcing resolutions across the land-sea continuum [in preparation]*.

Saint-Amand, A., Lambrechts, J., Thomas, C. J., & Hanert, E. (2023). How fine is fine enough? effect of mesh resolution on hydrodynamic simulations in coral reef environments. *Ocean Modelling*, *186*, 102254. https://doi.org/https://doi.org/10.1016/j.ocemod.2023.102254

Seneviratne, S., Zhang, X., Adnan, M., Badi, W., Dereczynski, C., Di Luca, A., Ghosh, S., Iskandar, I., Kossin, J., Lewis, S., Otto, F., Pinto, I., Satoh, M., Vicente-Serrano, S., Wehner, M., & Zhou, B. (2021). Weather and climate extreme events in a changing climate. In V. Masson-Delmotte, P. Zhai, A. Pirani, S. Connors, C. Péan, S. Berger, N. Caud, Y. Chen, L. Goldfarb, M. Gomis, M. Huang, K. Leitzell, E. Lonnoy, J. Matthews, T. Maycock, T. Waterfield, O. Yelekçi, R. Yu, & B. Zhou (Eds.), *Climate change 2021: The physical science basis. contribution of working group i to the sixth assessment report of the intergovernmental panel on climate change* (pp. 1513–1766). Cambridge University Press. https://doi.org/10.1017/9781009157896.013

Smagorinsky, J. (1963). General circulation experiments with the primitive equations: I. the basic experiment. *Monthly Weather Review*, *91*(3), 99–164. https://doi.org/10.1175/1520-0493(1963)091<0099:GCEWTP>2.3.CO;2

Sterckx, K., Delandmeter, P., Lambrechts, J., Deleersnijder, E., Verburg, P., & Thiery, W. (2023). The impact of seasonal variability and climate change on lake tanganyika's hydrodynamics. *Environmental Fluid Mechanics*. https://doi.org/10.1007/s10652-022-09908-8

Sterl, A. (2017). *Drag at high wind velocities – a review* (tech. rep. No. TR-361) (Accessed: 26-12-2024). Royal Netherlands Meteorological Institute (KNMI). https://cdn.knmi.nl/knmi/pdf/bibliotheek/knmipubTR/TR361.pdf

Steven, A. D. L., Baird, M. E., Brinkman, R., Car, N. J., Cox, S. J., Herzfeld, M., ..., & Yu, J. (2019). Ereefs: An operational information system for managing the great barrier reef. *Journal of Operational Oceanography*, *12*(sup2), S12–S28. https://doi.org/10.1080/1755876X.2019.1650589

Stewart, A., Frank, C., Justin, F., Diana, G., & Eric, S. (2018). A first-generation national storm surge forecast system ["January 2018"]. https://trove.nla.gov.au/work/233378585

Taylor, H. T., Ward, B., Willis, M., & Zaleski, W. (2010). The saffir-simpson hurricane wind scale. *Atmospheric Administration: Washington, DC, USA*.

Tellman, B., Sullivan, J. A., Kuhn, C., Kettner, A. J., Doyle, C. S., Brakenridge, G. R., Erickson, T. A., & Slayback, D. A. (2021). Satellite imaging reveals increased proportion of population exposed to floods. *Nature*, *596*(7870), 80–86. https://doi.org/10.1038/s41586-021-03695-w

Wolanski, E., Petus, C., Lambrechts, J., Brodie, J., Waterhouse, J., & Tracey, D. (2021). The intrusion of polluted fly river mud into torres strait. *Marine Pollution Bulletin*, *166*, 112243. https://doi.org/10.1016/j.marpolbul.2021.112243

UNIVERSITÉ CATHOLIQUE DE LOUVAIN
École polytechnique de Louvain
Rue Archimède, 1 bte L6.11.01, 1348 Louvain-la-Neuve, Belgique | **www.uclouvain.be/epl**